METHODS OF PIEZOELECTRIC ENERGY HARVESTING FROM HUMAN BODY MOTIONS

A Thesis
Presented to
The Academic Faculty

by

Bharat Kathpalia

In Partial Fulfillment
of the Requirements for the Degree
Master of Science in the
George W. Woodruff School of Mechanical Engineering

Georgia Institute of Technology
December 2018

METHODS OF PIEZOELECTRIC ENERGY HARVESTING FROM HUMAN BODY MOTIONS

Approved by:

Dr. Alper Erturk, Advisor
School of Mechanical Engineering
Georgia Institute of Technology

Dr. Ilan Stern, Advisor
Aerospace, Transportation and Advanced Systems Laboratory, Georgia Tech Research Institute

Dr. Karim G. Sabra
School of Mechanical Engineering
Georgia Institute of Technology

Date Approved: November 20, 2018

ACKNOWLEDGEMENTS

I would like to thank many people who guided, encouraged and supported me over the past three years for my graduate studies at Georgia Tech. First and foremost, I would like to offer my sincerest gratitude to my advisors, Professor Alper Erturk and Dr. Ilan Stern, for being my research mentors and their great help, guidance and advice towards completing this degree. I would also like to thank Professor Karim Sara, for reviewing my work, giving helpful advice and sharing his constructive criticism.

This work was supported by project D7762.0.0.0.0 sponsored by Delaware North Corporation (DNC) at NASA's Kennedy Space Center (KSC) and the Georgia Tech Research Institute's (GTRI) STEM Program, project N5116.6.0.7.0. I had the pleasure of working with past and present members of the Energy and Sustainability Laboratory at GTRI as well as the Smart Structures and Dynamical Systems Laboratory at Georgia Tech. I learned a lot from our group meetings and would like to thank them for their insight and suggestions. I would especially like to David Tan for his guidance and assistance with experimental setups and for volunteering to be the subject for my measurements.

Finally, I would like to thank my parents for their endless support of my endeavors.

TABLE OF CONTENTS

LIST OF TABLES

LIST OF FIGURES

SUMMARY

A lot of research has been done to enable self-powered wireless electronic devices. One of the most studied methods is the conversion of ambient vibrational energy into low-power electricity. The drastic decrease in power requirements of wearable electronics and sensors over the past decade makes the wearable devices industry a great test bed for this research. The growing interest in health and fitness monitoring, or even performance trackers in different sports provides many applications for this research. Smart flooring systems with Internet of Things integration have also received increased interest for tracking, security, and healthcare application. This work explores the potential of human-scale motion energy to enable self-powered sensor networks for on-body devices and potentially for indoor and outdoor smart flooring concepts. Electromechanical models are developed and analyzed for energy harvesting from base-excited and plucked bimorph piezoelectric cantilevers, as well as direct force excitation of curved unimorph harvesters. This thesis discusses the development and experimental validation of these models. Using measured human body acceleration and forces, the potential for energy harvesting from human motion using piezoelectric harvesters is quantified through experiments and model simulations.

CHAPTER 1. INTRODUCTION

1.1 Vibrational energy harvesting

The conversion of ambient vibrational energy into low-power electricity for enabling self-powered wireless electronic components has been widely researched over the last decade [1-6]. The domain of wearable electronics and sensors is also a growing field of research, with special focus on applications like fitness and health monitoring as well as wearable equipment that tracks performance in sports. Depending on usage amount, current consumer electronics with wireless communication functionality have an average power consumption between 17.7 mW and 110 mW, with a total energy consumption between 1529 J and 9504 J over the course of a 24 hour period [7]. Table 1 shows the peak power requirement of various electronic devices[8]. Energy harvester technologies target devices in the 10 nW to 100 mW range of power consumption. Additionally, smart flooring systems with Internet of Things integration are receiving increased interest for tracking, security and healthcare applications. This work explores the intersection of these emerging fields – the potential of human-scale motion energy to enable self-powered sensor networks for on-body devices and even indoor and outdoor smart flooring concepts.

Table 1 – Peak power requirements for various electronic devices [8]

Electronic Device	Peak Power	Electronic Device	Peak Power
Real Time Clock	100 nW	Bluetooth Transceiver	10 mW
Watch/Calculator	1 μW	GPS	100 mW
RFID Tag	10 μW	GSM Cell Phones	1 W
Sensors/Remotes	100 μW	Laptop Computer	10 W
Hearing Aids/Wireless Sensors	1 mW	Power tools	100 W

The methods of vibration-to-electric energy conversion include electromagnetic [9, 10], electrostatic [11, 12], and piezoelectric [13-17] transduction techniques. The use of magnetostriction [18, 19], electroactive polymers [20, 21], electret configurations [2, 22] and even flexoelectricity [23, 24] have also been explored. Due to the large power density of piezeoelectric materials and relative ease of application, piezoelectric transduction has received the highest attention of these techniques. The voltage outputs in electromagnetic energy harvesting are usually very low which limits the ability to charge a storage component which necessitates multi-stage post-processing to reach a usable input voltage or charge. Size of the harvester quickly becomes a limitation for generating usable levels of power. In piezoelectric energy harvesting, however, usable voltage output can be obtained directly from the harvester, and through different harvesting architectures the excitations can be tuned to maximize the electrical output from the same volume of harvester. Piezoelectric devices can also be fabricated in micro-scale applications using well established thick and thin-film fabrication techniques [3].

1.2 Piezoelectric energy harvesting using human motion

Many research groups have explored human motion energy harvesting using piezoelectric transduction. In early literature, Shenck and Paradiso [15] investigated harvesting energy from the deformation of a shoe sole and from the heel strike during walking. Comparing the output of a polyvinylidene fluoride (PVDF) stave, curved unimorph harvester and a compressible dimorph, they were able to transmit radio-frequency identification (RFID) signals using harvested power. More recently, Moro and Benasciutti [17, 25] studied the energy harvesting potential of the human gait by mounting a piezoelectric bimorph cantilever in the heel of a running shoe. Initial experimental results showed a maximum of 13 μW per footstep, but with optimization of the bimorph configuration it was possible to achieve 395 μW per footstep. This experimentation confirms that there is merit in studying the human gait, and that heel acceleration alone could result in significant energy harvesting. However, to successfully tune a piezoelectric harvester to the low frequencies inherent to ambient vibrations and human motion would commonly require large dimensions or proof mass. This issue can be avoided by implementing frequency-up conversion mechanisms. These include plucking mechanisms, like the one explored by Pozzi and Zhu [26, 27] in their knee-joint energy harvester, magnetic plucking [28, 29], impact mechanisms [30], and even non-linear secondary resonance [31, 32].

Another next-generation application of piezoelectric transduction is to enable indoor and outdoor smart flooring and energy recovery from human locomotion. The motivation varies from sensing applications for tracking and security in high foot traffic areas and use as an additional source of markers in healthcare facilities to energy recovery

from vehicular or human movement on roadways and pavements. Most designs for these applications employ piezoelectric elements under compressive forces. Others utilize piezoelectric layers on a cantilevered beam host structure [33-35]. One approach to efficiently enabling and integrating smart flooring is discrete flooring tiles with energy harvesting and Internet of Things (IoT) capability [36, 37].

1.3 Outline of the thesis

This work explores various methods of piezoelectric energy harvesting from human body motions and looks at developing harvesting architectures for both on-body as well as flooring applications. Chapter 2 focuses on understanding the acceleration and force levels associated with human motion. Three activity levels are chosen: walking (3 mph), jogging (5 mph), and sprinting (7 mph). These acceleration and force levels are analyzed for periodicity and represented using Fourier series expressions, which later serve as the input to the models for different harvesters. Chapter 3 establishes the models developed for the different energy harvesting architectures explored in this work. First, the electromechanical model for a cantilevered piezoelectric bimorph harvester developed by Erturk and Inman [5] is reviewed. Next, this model is extended to periodic base excitation. The harvester electromechanical model is coupled with a model that is developed for non-linear plectrums to predict the electrical and mechanical response of a harvester to plucking excitation. Lastly, an electromechanical model for curved unimorph harvesters is discussed. Chapter 4 provides experimental validations for the analytical models described in chapter 3. Experiments are performed using two types of harvesters: a Piezo Systems, Inc bimorph and a FACE International Corporation THUNDER® harvester. The experiments focus on an excitation frequency range of 1-10 Hz, to capture the frequencies

associated with human motion and ambient vibration, and are performed over a range of load resistances. Finally, the last chapter discusses the conclusions and provides recommendations for future work in this field.

CHAPTER 2. MEASUREMENT OF HUMAN BODY ACCELERATION AND FORCES

In order to understand the acceleration levels on the human body and force levels imparted on the floor during human motion, a series of data collection trials was run to quantify excitation levels for both wearable as well as floor-based applications. The acceleration data is of interest for base-excited cantilevered piezoelectric energy harvesters, while the force data is of interest for shoe-mounted curved piezoelectric energy harvesters in the context of this work. The measured acceleration and force levels are to be used in the electromechanical models of piezoelectric energy harvesting methods to be developed in the next chapter. The trial cases were chosen to represent walking (3 mph), jogging (5 mph) and sprinting (7 mph). In terms of kinematic measurements (to quantify displacement and acceleration), the body parts chosen for this analysis were the wrist and ankle as they have the largest range of motion during human movement, and high energy fluctuations as compared to other parts of the body. The forces measured were those exerted by the human body onto the floor. The following summarizes the experimental measurement of these data by using a triaxial accelerometer and by means of a motion camera system.

2.1 Acceleration Measurements Using a Triaxial Accelerometer

For base-excited wearable energy harvesting applications, the focus is placed on using the acceleration of different body parts during regular movements, specifically for regions of maximum acceleration. The acceleration measurements were taken using an accelerometer strapped to a subject as shown in Figure 1. Speed of motion was controlled

using a treadmill. Figure 2 shows acceleration histories on human ankle associated with walking, jogging, and sprinting in terms of the gravitation acceleration g. The peak acceleration levels seen were as high as several g's.

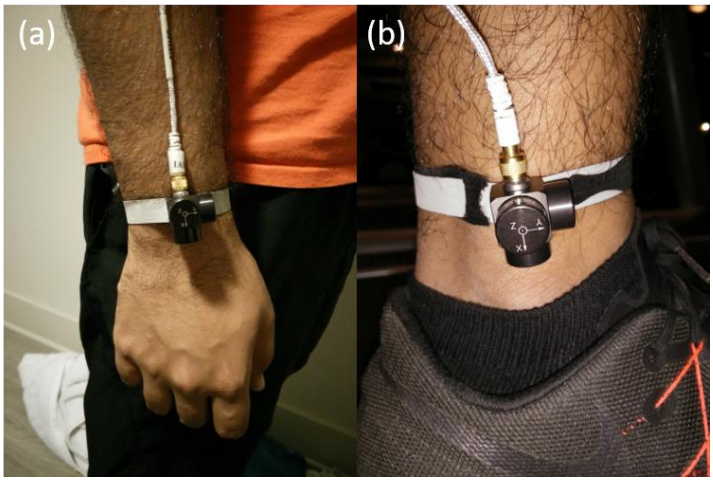

Figure 1 – Triaxial accelerometer strapped to the (a) wrist and (b) ankle of a subject

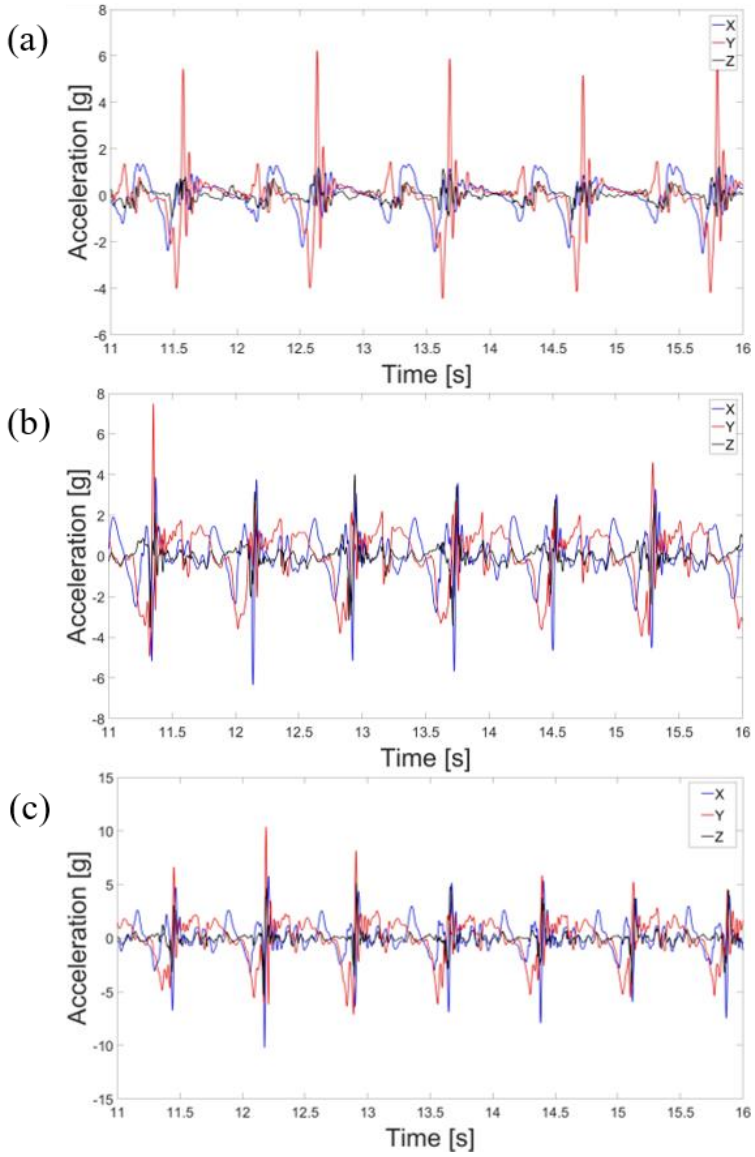

Figure 2 – Various acceleration histories measured on human ankle during (a) walking, (b) jogging, and (c) sprinting

In the electromechanical modeling and analysis sections of this thesis, it will be assumed that the acceleration and force associated with human motion is periodic. Therefore, the experimental data reported in this chapter can be approximated as periodic. A function is said to be periodic if it satisfies the condition outlined by Equation (1), where T is the period of the function.

$$a(t) = a(t+T) \tag{1}$$

The Fourier series expansion of a periodic base acceleration can be expressed as

$$a(t) = p_0 + \sum_{k=1}^{\infty}\left[p_k \cos\left(k\frac{2\pi t}{T}\right) + q_k \sin\left(k\frac{2\pi t}{T}\right)\right] \tag{2}$$

where p_0 is the mean value of the function, and p_k, q_k are the Fourier coefficients. These values can be calculated using:

$$p_0 = \frac{1}{T}\int_0^T a(t)dt \tag{3}$$

$$p_k = \frac{2}{T}\int_0^T a(t)\cos\left(k\frac{2\pi t}{T}\right)dt \tag{4}$$

$$q_k = \frac{2}{T}\int_0^T a(t)\sin\left(k\frac{2\pi t}{T}\right)dt \tag{5}$$

where k are positive integers. Following the Fourier series expansion of the base acceleration, two approximations are made to truncate the expression. First, using only the number of terms required to ensure convergence, the summation of harmonics can be truncated after taking N harmonic pairs. Second, considering periodic acceleration fluctuation in most physical systems, the constant segment of the expansion can be

neglected by setting p_0 = 0. The truncated form of the Fourier series expansion now represents the acceleration using only harmonic functions: [5]

$$a(t) \cong \sum_{k=1}^{N} \left[p_k \cos\left(k \frac{2\pi t}{T} \right) + q_k \sin\left(k \frac{2\pi t}{T} \right) \right] \tag{6}$$

Figure 3 shows the measured time series represented using the Fourier series expansion method described above. These expressions are used as an input to predict the electromechanical response of piezoelectric harvesters. Note that the experimental time series is never perfectly periodic yet using a single period and expanding the series accordingly is still a good approximation. While a single period analysis can be deemed sufficient, the entire time history of data from experiments (involving multiple periods) is taken as the function to be analyzed in Fourier series throughout the thesis since it is computationally affordable. It is important to notice that most of the frequency content of these acceleration histories is in the 0-5 Hz range, which would be the expected frequency range for human motion.

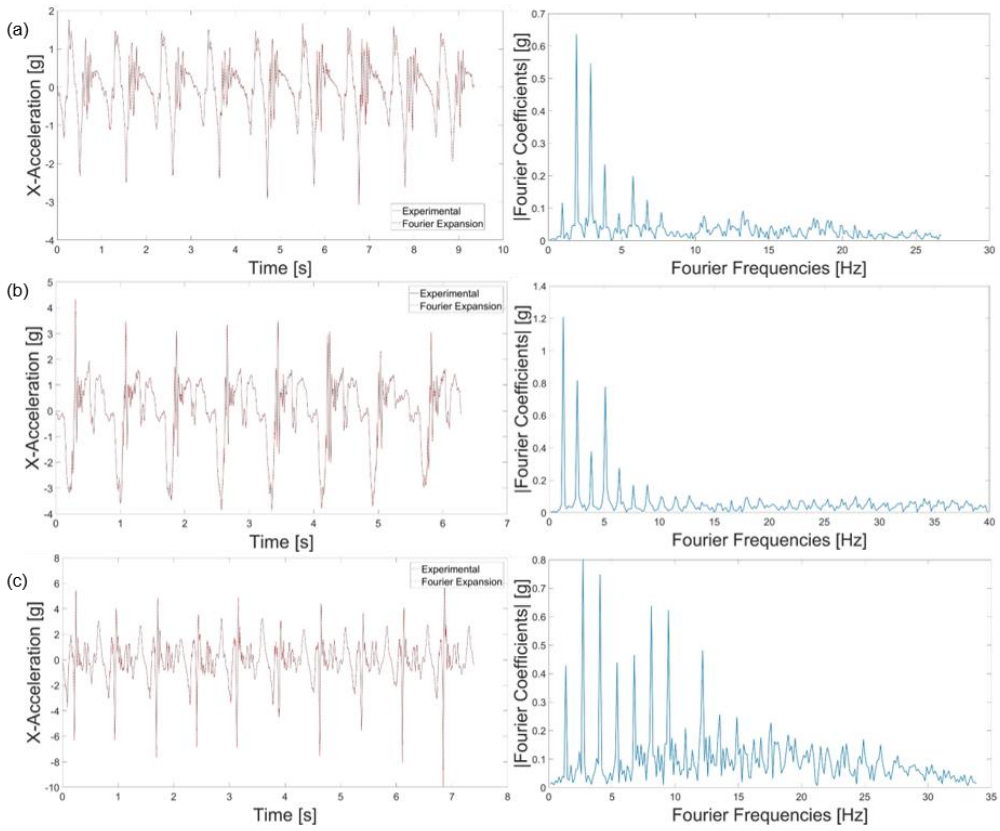

Figure 3 – Fourier series (with Fourier coefficients vs. Fourier frequencies) representation of the acceleration time series associated with (a) walking, (b) jogging, and (c) sprinting

2.2 Force and Acceleration Measurements Using Motion Capture Cameras

For floor-based vibrational energy harvesters/sensors and for shoe-inserted harvesters, the forces exerted by human motion on floors are of interest. The positions of 44 points on the human body in motion were recorded during motion to understand the relationship between these forces and the acceleration. These measurements were taken using an instrumented treadmill operating at the same speeds as before combined with motion capture cameras shown in Figure 4. Figure 5 shows the simultaneous force and acceleration measurements and Figure 6 shows a sample of the motion capture data plotted in 3D. Since the acceleration data was already obtained as shown in the previous figure

with a better sampling frequency, only the force data will be used from the motion capture analysis. A similar Fourier series approximation can be performed on the force data as shown in Figure 7.

Figure 4 – Instrumented treadmill and motion capture targets on subject

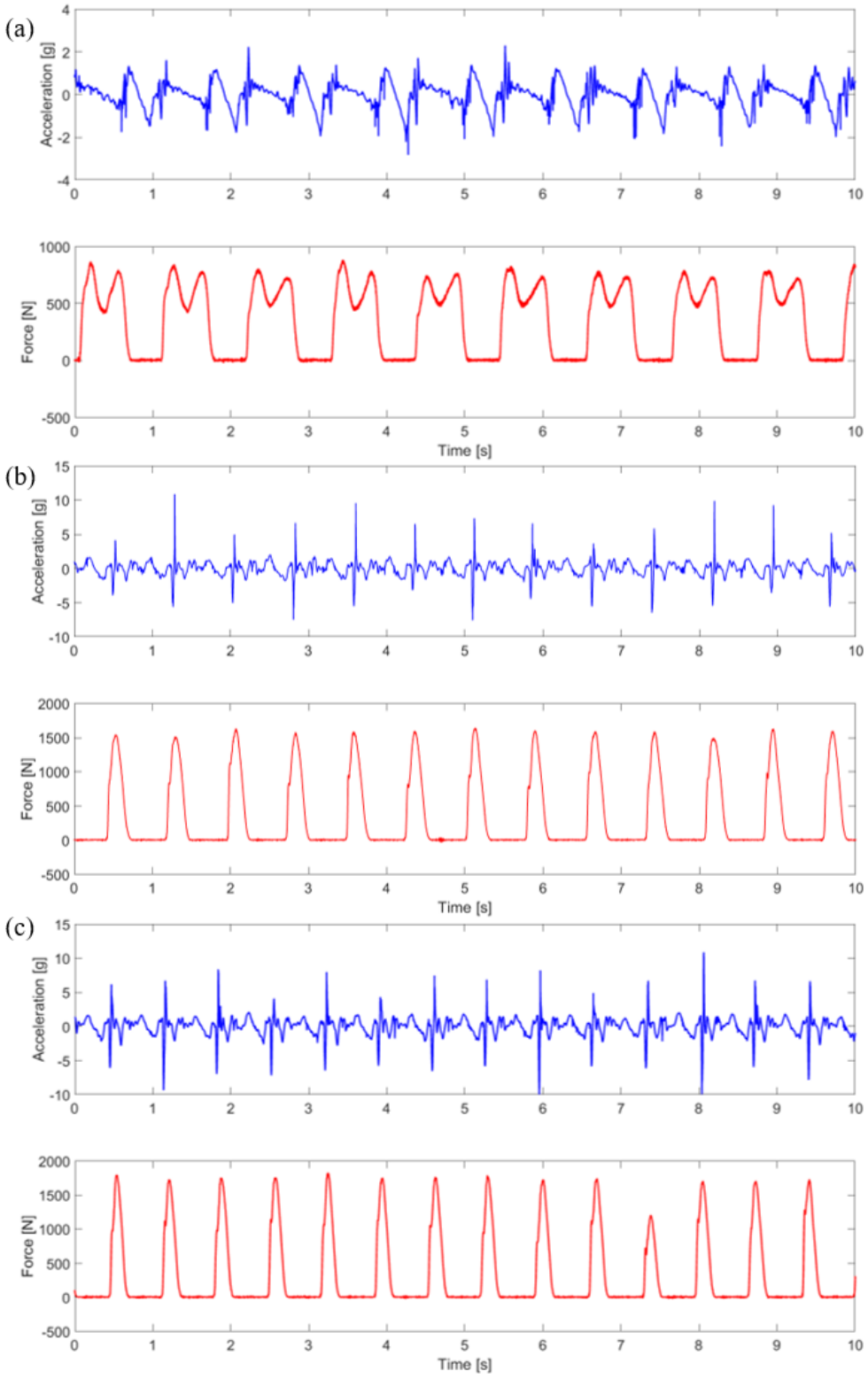

Figure 5 – Acceleration and force histories measured during (a) walking, (b) jogging, (c) sprinting

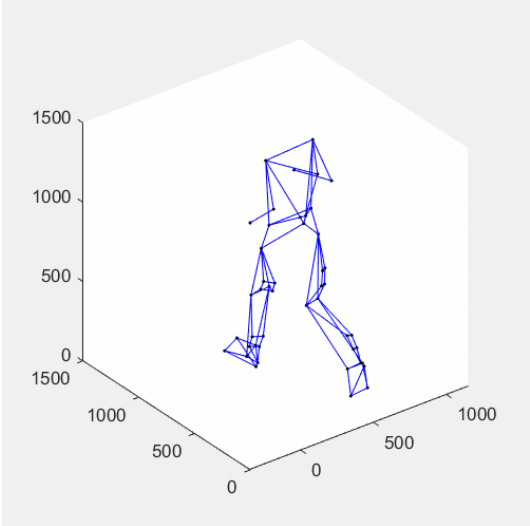

Figure 6 – Sample output of motion capture data plotted in 3D

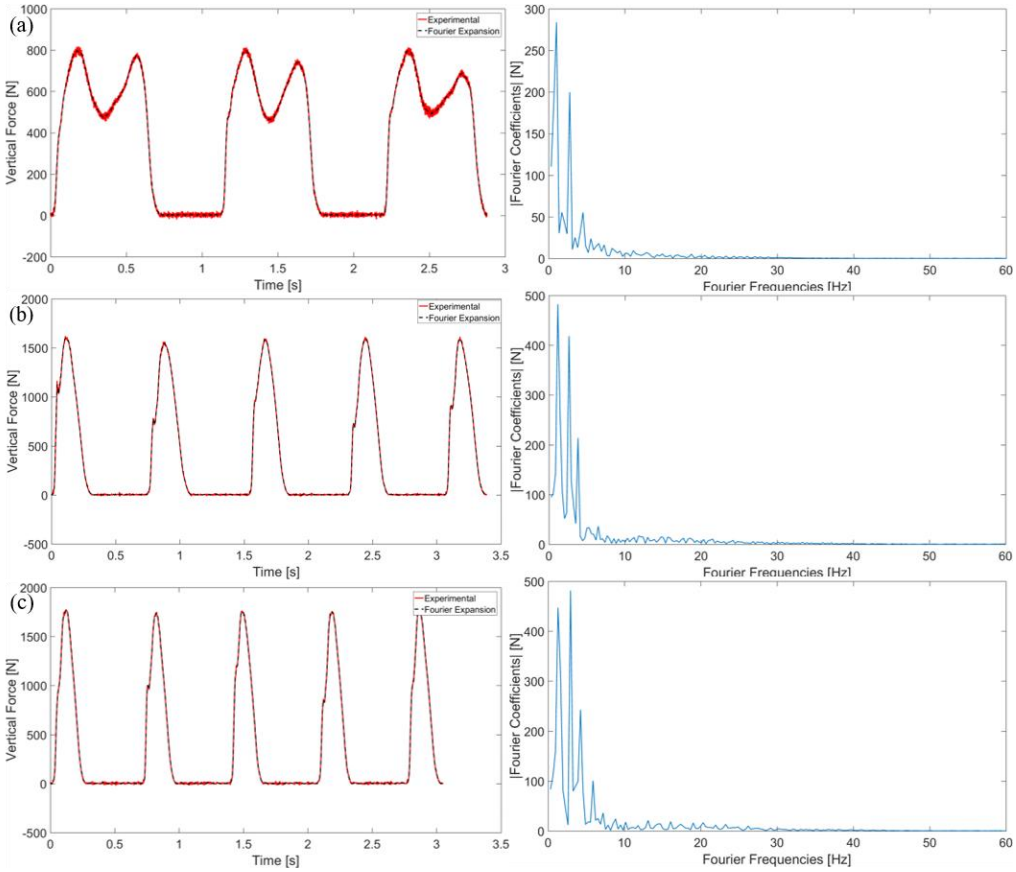

Figure 7 – Fourier series (with Fourier coefficients vs. Fourier frequencies) representation of the force time series associated with (a) walking, (b) jogging, and (c) sprinting

CHAPTER 3. DEVELOPING ELECTROMECHANICAL MODELS FOR VARIOUS PIEZOELECTRIC HARVESTERS

This chapter presents electromechanical models for various piezoelectric energy harvesting approaches explored in this work. First, the electromechanical model for a cantilevered piezoelectric bimorph harvester developed by Erturk and Inman [5] is reviewed. Here the frequency dependent voltage and vibration response to base acceleration is defined. This model is then extended to periodic excitation to predict the electrical and mechanical response for a given load resistance. Plucking excitation of a cantilevered piezoelectric energy harvester is also discussed with a new modeling approach that accounts for the plectrum's geometric nonlinearity. This model also establishes the relationships between key system parameters, such as the plectrum thickness and overlap length and the overall harvester power. These relationships are explored, and methods for maximization of power output or system optimization are described. Finally, the electromechanical model for a curved unimorph harvester is developed. Using the off-resonance excitation of a piezoelectric stack as a foundation, this model is used to predict the electrical response of a curved unimorph harvester for given forcing amplitudes and frequencies.

3.1 Electromechanical Modeling of a Base-Excited Piezoelectric Energy Harvester

This section reviews the electromechanical model of a base-excited piezoelectric energy harvester derived by Erturk and Inman [5]. It is assumed that the base acceleration,

$a(t)$ is translational and the rotation term at the base of the harvester is neglected as shown in Figure 8.

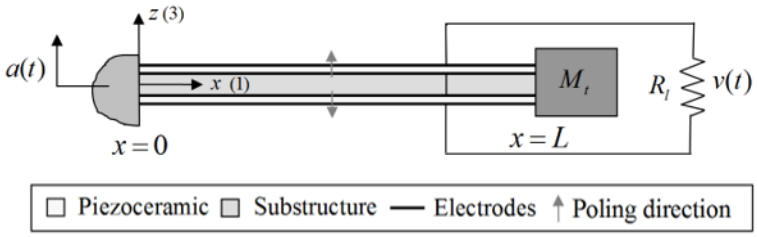

Figure 8 – Cantilevered bimorph piezoelectric energy harvester in series configuration under base excitation[5]

The dynamics of a cantilevered bimorph piezoelectric harvester under base excitation are governed by,

$$YI\frac{\partial^4 w_{rel}(x,t)}{\partial x^4}+c_s I\frac{\partial^5 w_{rel}(x,t)}{\partial x^4\partial t}+c_a\frac{\partial w_{rel}(x,t)}{\partial t}+m\frac{\partial^2 w_{rel}(x,t)}{\partial t^2}-\vartheta v(t)\left[\frac{d\delta(x)}{dx}-\frac{d\delta(x-L)}{dx}\right]= -\left[m+M_t\delta(x-L)\right]a(t) \tag{7}$$

$$C_{\tilde{p}}^{eq}\frac{dv(t)}{dt}+\frac{v(t)}{R_l}+\vartheta\int_0^L\frac{\partial^3 w_{rel}(x,t)}{\partial x^2\partial t}dx=0 \tag{8}$$

where $w_{rel}(x,t)$ is the transverse displacement of the neutral axis relative to moving base at position *x* and time *t*, $v(t)$ is the voltage response across the external resistive load R_l, c_a is the viscous air damping coefficient, $c_s I$ is the effective strain-rate damping coefficient for the composite structure), *m* is the mass per unit length of the beam, M_t is a tip mass, $C_{\tilde{p}}^{eq}$ is the equivalent capacitance of the piezoceramic layers, ϑ is the

electromechanical coupling term in the physical coordinates and $\delta(x)$ is the Dirac delta function. For the series configuration of the bimorph, the electromechanical coupling term is $\vartheta = \bar{e}_{31} b h_{\tilde{p}c}$, where $\bar{e}_{31}$ is the plane-stress piezoelectric stress constant, *b* is the width of the layers, and $h_{\tilde{p}c}$ is the distance from the neutral axis to the center of each piezoceramic layer.

Equation (9) expresses the vibration response in terms of the modal coordinates $\eta_r(t)$ and the mode shapes $\phi_r(x)$, derived using standard modal analysis procedures.

$$w_{rel}(x,t) = \sum_{r=1}^{\infty} \phi_r(x) \eta_r(t) \tag{9}$$

Equations (7) and (8) can be represented using these modal coordinates and reduced to the following electromechanically coupled ordinary differential equations:

$$\frac{d^2\eta_r(t)}{dt^2} + 2\zeta_r \omega_r \frac{d\eta_r(t)}{dt} + \omega_r{}^2 \eta_r(t) - \tilde{\theta}_r v(t) = \sigma_r a(t) \tag{10}$$

$$C_{\tilde{p}}^{eq} \frac{dv(t)}{dt} + \frac{v(t)}{R_l} + \sum_{r=1}^{\infty} \tilde{\theta}_r \frac{d\eta_r(t)}{dt} = 0 \tag{11}$$

where ω_r is the undamped natural frequency in short-circuit (i.e. constant electric field) conditions, ζ_r is the modal mechanical damping ratio, σ_r is a modal forcing related term and $\tilde{\theta}_r$ is the modal electromechanical coupling.

For the case of harmonic base acceleration, $a(t) = A_0 e^{j\omega t}$, the steady-state analytical solution for the voltage -to- base acceleration frequency response function (FRF) is given by:

$$\alpha(\omega) = \frac{v(t)}{A_0 e^{j\omega t}} = \frac{\sum_{r=1}^{\infty} \frac{-j\omega\tilde{\theta}_r \sigma_r}{\omega_r{}^2 - \omega^2 + j2\zeta_r\omega_r\omega}}{\frac{1}{R_l} + j\omega C_{\tilde{p}}^{eq} + \sum_{r=1}^{\infty} \frac{j\omega\tilde{\theta}_r^2}{\omega_r{}^2 - \omega^2 + j2\zeta_r\omega_r\omega}} \tag{12}$$

and the steady-state vibration response -to- base acceleration FRF is:

$$\beta(\omega, x) = \frac{w_{rel}(x,t)}{A_0 e^{j\omega t}} = \sum_{r=1}^{\infty} \left[\left(\sigma_r - \tilde{\theta}_r \frac{\sum_{r=1}^{\infty} \frac{j\omega\tilde{\theta}_r \sigma_r}{\omega_r{}^2 - \omega^2 + j2\zeta_r\omega_r\omega}}{\frac{1}{R_l} + j\omega C_{\tilde{p}}^{eq} + \sum_{r=1}^{\infty} \frac{j\omega\tilde{\theta}_r^2}{\omega_r{}^2 - \omega^2 + j2\zeta_r\omega_r\omega}} \right) \frac{\phi_r(x)}{\omega_r{}^2 - \omega^2 + j2\zeta_r\omega_r\omega} \right] \tag{13}$$

3.2 Periodic Base Excitation of a Cantilevered Piezoelectric Energy Harvester

If the base acceleration is harmonic of the form given by Equation (1), then, based on the theory reviewed in Section 3.1, the periodic voltage output can be expressed as

$$v(t) \cong \sum_{k=1}^{N} \left| \alpha\left(k\frac{2\pi}{T} \right) \right| \left\{ p_k \cos\left[\left(k\frac{2\pi t}{T} \right) + \Phi\left(k\frac{2\pi}{T} \right) \right] + q_k \sin\left[\left(k\frac{2\pi t}{T} \right) + \Phi\left(k\frac{2\pi}{T} \right) \right] \right\} \tag{14}$$

where $|\alpha(\omega)|$ is the amplitude and $\Phi(\omega)$ is the phase of the voltage output – to – base acceleration FRF for a given load resistance as defined in the previous section. The periodic power output can be obtained from the following expression:

$$P(t) \cong \frac{1}{R_l}\left\langle \sum_{k=1}^{N} \left| \alpha\left(k\frac{2\pi}{T}\right) \right| \left\{ p_k \cos\left[\left(k\frac{2\pi t}{T}\right) + \Phi\left(k\frac{2\pi}{T}\right)\right] + q_k \sin\left[\left(k\frac{2\pi t}{T}\right) + \Phi\left(k\frac{2\pi}{T}\right)\right] \right\} \right\rangle^2 \quad (15)$$

Finally, the tip displacement – to – base acceleration FRF reviewed in the previous section can be used to simulate the periodic vibration response of the energy harvester for a given electrical load:

$$w(x,t) \cong \sum_{k=1}^{N} \left| \beta\left(k\frac{2\pi}{T}, x\right) \right| \left\{ p_k \cos\left[\left(k\frac{2\pi t}{T}\right) + \Psi\left(k\frac{2\pi}{T}, x\right)\right] + q_k \sin\left[\left(k\frac{2\pi t}{T}\right) + \Psi\left(k\frac{2\pi}{T}, x\right)\right] \right\} \quad (16)$$

which can be used for the mechanical design and stress analysis purposes.

3.3 Plucked Piezoelectric Bimorph Harvester for Frequency-Up Conversion

Another energy harvesting architecture of interest is the plucking of a linear (stiff) piezoelectric bimorph harvester using a geometrically non-linear (flexible) plectrum [38]. The goal is to enable frequency-up conversion of low frequency ambient vibrations or human motion to the resonant frequency of the harvester. The assumption for the development of this model is that the plectrum exhibits large enough deformations to achieve the plucking excitation while the piezoelectric bimorph is relatively stiff and undergoes small oscillations. Figure 9 is a schematic that describes the frequency-up conversion process, where the overlap length *d* and the release height *h* are critical parameters that relate the axial shortening associated with bending deformation.

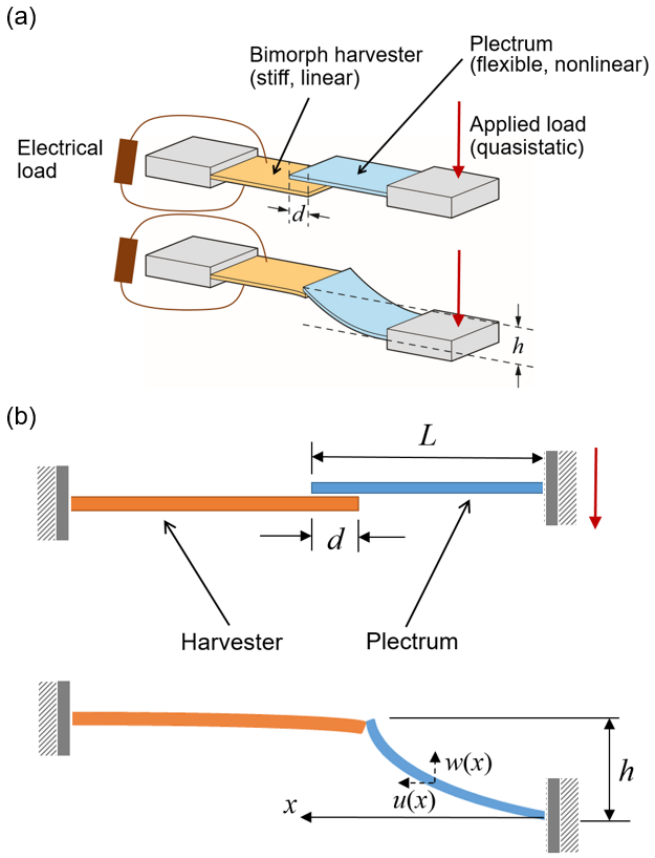

Figure 9 – (a) Schematic of plucking based frequency-up conversion mechanism using a geometrically non-linear plectrum and a linear piezoelectric bimorph energy harvester and (b) relevant geometric parameters

To define the relationship between the overlap length *d* and the release height *h* for a given plectrum length *L*, a geometrically non-linear model for the quasistatic flexible plectrum deformation based on the von Kármán theory is implemented. The homogenous differential equations governing the static deflection of a thin cantilever (flexible plectrum in Figure 9) with von Kármán – type geometric nonlinearity [39] can be derived from

$$\frac{dN}{dx} = 0 \tag{17}$$

$$\frac{d^2M}{dx^2} + \frac{d}{dx}\left(N \frac{dw}{dx} \right) = 0 \tag{18}$$

where the axial force resultant (N) and the bending moment (M) terms can be expressed as

$$N(x) = EA\left[\frac{du}{dx} + \frac{1}{2}\left(\frac{dw}{dx} \right)^2 \right] \tag{19}$$

$$M(x) = -EI \frac{d^2w}{dx^2} \tag{20}$$

In Equations (27) and (28), *u* and *w* are the longitudinal and transverse displacement variables seen in Figure 9, *EA* is the axial rigidity and *EI* is the flexural rigidity of the plectrum. Substituting Equations (27) and (28) into Equation (29), the transverse shear force resultant term can be expressed as

$$Q(x) = \frac{dM}{dx} + N \frac{dw}{dx} = -\frac{d}{dx}\left(EI \frac{d^2w}{dx^2} \right) + EA\left[\frac{du}{dx} + \frac{1}{2}\left(\frac{dw}{dx} \right)^2 \right] \frac{dw}{dx} \tag{21}$$

The boundary conditions for the clamped ($x = 0$) end of the clamped-free plectrum beam with a transversely applied force (P) at the free end are

$$u(0) = 0 \tag{22}$$

$$w(0) = 0 \tag{23}$$

$$\left.\frac{dw}{dx}\right|_{x=0} = 0 \tag{24}$$

While the boundary conditions at the free ($x = L$) end are

$$N(L) = EA\left[\frac{du}{dx} + \frac{1}{2}\left(\frac{dw}{dx}\right)^2\right]_{x=L} = 0 \tag{25}$$

$$M(L) = -EI\left.\frac{d^2w}{dx^2}\right|_{x=L} = 0 \tag{26}$$

$$Q(L) = \left[\frac{dM}{dx} + N\frac{dw}{dx}\right]_{x=L} = \left\{-\frac{d}{dx}\left(EI\frac{d^2w}{dx^2}\right) + EA\left[\frac{du}{dx} + \frac{1}{2}\left(\frac{dw}{dx}\right)^2\right]\frac{dw}{dx}\right\}_{x=L} = -P \tag{27}$$

At the instant of the release, this quasistatic transverse tip force is the same tip force acting on the harvester and yields the initial displacement for the plucking motion.

Equation (17) implies that the resultant axial force is constant ($N(x) = C$) at every point on the plectrum. Furthermore, the boundary condition represented in Equation (25) states that the axial force is 0 at the tip, $N(L) = 0$. Therefore, $N(x) = 0$ at all points along the length of the plectrum. Combing this result with Equation (19), it can be stated that

$$\frac{du}{dx} = -\frac{1}{2}\left(\frac{dw}{dx}\right)^2 \tag{28}$$

Applying the boundary condition represented in Equation (22) to Equation (28),

$$u(x) = -\frac{1}{2}\int_0^x \left(\frac{dw}{dx}\right)^2 dx \tag{29}$$

Considering the flexural rigidity of the uniform plectrum is constant ($EI = C$) and using Equation (29); the boundary condition represented in Equation (27) can be reduced to

$$-EI\left.\frac{d^3w}{dx^3}\right|_{x=L} = P \tag{30}$$

Using the boundary conditions in Equations (23), (24), (25) and (30), the transverse beam deflection can be expressed in terms of the applied force

$$w(x) = \frac{P}{6EI}\left(3Lx^2 - x^3\right) \tag{31}$$

which yields,

$$\frac{dw}{dx} = \frac{P}{2EI}\left(2Lx - x^2\right) \tag{32}$$

Substituting Equation (32) into Equation (29) results in

$$u(x) = -\frac{1}{8}\left(\frac{P}{EI}\right)^2 \int_0^x \left(2L\eta - \eta^2\right)^2 d\eta = -\frac{1}{8}\left(\frac{P}{EI}\right)^2 \int_0^x \left(4L^2\eta^2 - 4L\eta^3 + \eta^4\right) d\eta$$
$$= -\frac{1}{8}\left(\frac{P}{EI}\right)^2 \left(\frac{4L^2x^3}{3} - Lx^4 + \frac{x^5}{5}\right) = -\left(\frac{P}{EI}\right)^2 \left(\frac{20L^2x^3 - 15Lx^4 + 3x^5}{120}\right) \quad (33)$$

Equation (31) can be rearranged to

$$\frac{P}{EI} = \frac{6w(x)}{3Lx^2 - x^3} \quad (34)$$

which when substituted into Equation (33) gives

$$u(x) = -\left(\frac{6w(x)}{3Lx^2 - x^3}\right)^2 \left(\frac{20L^2x^3 - 15Lx^4 + 3x^5}{120}\right) = -\frac{3}{10}\left(\frac{20L^2x^3 - 15Lx^4 + 3x^5}{9L^2x^4 - 6Lx^5 + x^6}\right) w^2(x) \quad (35)$$

Equation (35) defines the longitudinal deflection $u(x)$ of the plectrum in terms of a geometrically large deflection $w(x)$. The axial deflection at the free end of the plectrum caused by transverse deflection can be defined as

$$u(L) = -\frac{3}{5}\frac{w^2(L)}{L} \quad (36)$$

here $u(L) < 0$ irrespective of the sign of $w(L)$. Therefore,

$$w(L) = \sqrt{-\frac{5L}{3}u(L)} \tag{37}$$

Therefore, the tip deflection, h of the plectrum at the instant of release (release height in Figure 9) is

$$h = \sqrt{\frac{5}{3}dL} \tag{38}$$

where, d is the overlap length of the plectrum over the stiff harvester. Note that the transverse tip force P at the instant of release can be obtained by setting $x = L$ and $w(L) = h$.

Next, the electromechanical model for a linear piezoelectric energy harvester excited by the non-linear plectrum is developed. The bimorph harvester is considered much stiffer than the plectrum, and therefore its behavior can be approximated by the linear cantilevered bimorph piezoelectric energy harvester model developed by Erturk and Inman [5, 16].

Since tip deflection-based deformation is predominantly in the first bending mode, a single-mode solution for the vibration response is applied to the bimorph. This yields the following approximation:

$$w_h(L_h, t) = \sum_{r=1}^{\infty} \phi_r(L_h)\eta_r(t) \cong \phi_1(L_h)\eta_1(t) \tag{39}$$

where $w_h(L_h,t)$ is the transverse displacement of the bimorph harvester as a function of overhang length L_h and $\phi_1(L_h)$ is the mass normalized eigenfunction, derived from the Euler-Bernoulli beam theory, evaluated at the cantilever tip, and $\eta_1(t)$ is the modal coordinate. From here, the governing electromechanical equations for free vibrations are derived to be:

$$\frac{d^2 w_h(L_h,t)}{dt^2} + 2\zeta_1\omega_1 \frac{dw_h(L_h,t)}{dt} + \omega_1^2 w_h(L_h,t) - \theta_1\phi_1(L_h)v(t) = 0 \tag{40}$$

$$C_p \frac{dv(t)}{dt} + \frac{v(t)}{R_l} + \frac{\theta_1}{\phi_1(L_h)} \frac{dw_h(L_h,t)}{dt} = 0 \tag{41}$$

where C_p is the equivalent capacitance of the bimorph, R_l is the load resistance, $v(t)$ is the voltage across the resistance, ζ_1 is the viscous damping ratio, ω_1 is the natural frequency of the linear bimorph harvester for the first bending mode in short circuit, and θ_1 is the modal electromechanical coupling that depends on the cross-section and material parameters of the bimorph [5, 16].

The quasistatic plucking excitation creates the following initial conditions

$$w_h(L_h,0) = \frac{PL_h^3}{3EI_h} \tag{42}$$

$$\frac{dw_h(L_h,0)}{dt} = 0 \tag{43}$$

$$v(0) = 0 \tag{44}$$

where, EI_h is the flexural rigidity of the bimorph harvester and P is the transverse tip force on the harvester created by the plucking deflection *h* shown in Figure 9. This transverse tip force is the reaction force to the tip force seen in the plectrum from the previous section

$$P = \frac{3EI}{L^3}\sqrt{\frac{5}{3}dL} \tag{45}$$

It is assumed that the quasistatic external stimulus on the plectrum (due to human motion – walking, etc.) is large enough to create a plucked excitation. This can be checked by comparing the external load to the load at release calculated in Equation (45). Then Equations (40) and (41) can be written in the first order form and they can be simulated in the time domain using the initial conditions outlined in Equations (42)-(44).

3.4 Curved Unimorph Harvester under Direct Force Excitation

The THUNDER® consists of a thin thickness-poled piezoelectric wafer bonded to a steel substrate and an aluminum superstrate. Figure 10 is a schematic of the THUNDER® energy harvester and its loading scenario.

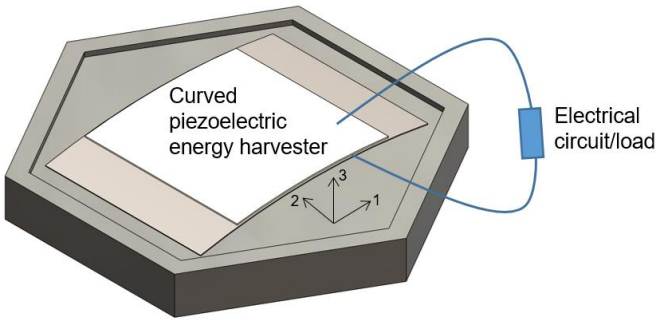

Figure 10 – Schematic of a THUNDER® energy harvester under direct force excitation (applied force is parallel to 3-axis)

The excitations considered for the electromechanical model of the THUNDER® transducers are low frequency (<10 Hz) to emulate human motion. An AC input – AC output model was developed for excitations at these frequencies. The two main assumptions for this model were (1) linear electromechanical behavior, i.e. linear piezoelectricity [40], and (2) off-resonant low-frequency behavior, i.e. the fundamental resonance frequency of the harvester is sufficiently higher that the excitation frequency content.

The governing low-frequency dynamics of a curved unimorph are similar to off-resonant excitation of piezoelectric stacks operating in the thickness mode (33-mode) [41]. The electric current flowing through a resistive load across the electrodes is obtained from: [5, 37]

$$\frac{d}{dt}\left(\int_A \mathbf{D}\cdot\mathbf{n}dA\right)=\frac{v(t)}{R_l} \tag{46}$$

where $\mathbf{D}$ is the vector of electric displacement components, $\mathbf{n}$ is the unit outward normal vector, $v(t)$ is the voltage output across the electrodes, R_l is the load resistance, and the integration is performed over the surface area of the electrode A. For the 31-mode of piezoelectricity, the relevant electric displacement component (D_3) is in the thickness direction (3- direction in Figure 10, perpendicular to the surface electrodes) and is represented by

$$D_3 = d_{31} S_1 + \varepsilon_{33}^s E_3 \tag{47}$$

where S_1 is the bending strain (in 1- direction), E_3 is the electric field (in 3- direction), d_{31} is the piezoelectric strain constant, and ε_{33}^s is the permittivity component at constant strain. Substituting Equation (47) into Equation (46) yields

$$C_p \dot{v}(t) + \frac{v(t)}{R_l} = \theta \frac{dF(t)}{dt} \tag{48}$$

where C_p is the internal capacitance of the piezoelectric element, θ is the electromechanical coupling term, and $F(t)$ is the dynamic vertical force applied to the harvester. The mechanical excitation applied to the harvester could also be represented in the form of the dynamic strain $S(t)$ in the piezoelectric layer (1- direction) or the dynamic radius of curvature $\rho(t)$ fluctuation. Thus, Equation (20) can also be represented as

$$C_p \dot{v}(t) + \frac{v(t)}{R_l} = \alpha \frac{dS(t)}{dt} \tag{49}$$

or

$$C_p \dot{v}(t) + \frac{v(t)}{R_l} = \beta \frac{d\rho(t)}{dt} \tag{50}$$

Note that θ, α, and β depend on the material and geometric parameters, and are related to each other, for example $S(t) = -h_{pc}\rho(t)$, where h_{pc} is the distance of the center of the piezoelectric layer's thickness from the neutral axis level in the 3- direction.

Assuming the force acting on the piezoelectric harvester, $F(t)$ is harmonic. The dynamic forcing can be expressed in the form:

$$F(t) = F_0 e^{j\omega t} \tag{51}$$

where F_0 is the magnitude of the force, ω is the frequency in rad/s, and j is the unit imaginary number. The steady state voltage response can now be expressed as

$$v(t) = V_0 e^{j\omega t} \tag{52}$$

Equations (51) and (52) can then be used to derive the complex voltage output – to – force input frequency response function (FRF)

$$\alpha(\omega) = \frac{V_0}{F_0} = \frac{j\omega\theta}{1/R_l + j\omega C_p} \tag{53}$$

which can be used to further express the power output – to – force input FRF

$$\Pi(\omega) = \left|\frac{V_0}{F_0}\right|^2 \frac{1}{R_l} = \frac{\omega^2\theta^2 R_l}{1+(\omega C_p R_l)^2} \tag{54}$$

Notice that the voltage output, $|V_0|$ is linearly proportional to the applied force amplitude $|F_0|$. Using the known relationship between power and voltage, $P(t) = v(t)^2/R_l$ there is a clear quadratic relationship between the power output and force input. At a given frequency, the optimal electrical load can be found as $R_{l,opt} = 1/\omega C_p$, for maximum power output can be calculated from Equation (54) by finding the maxima, $d\Pi/dR_l = 0$ [37].

CHAPTER 4. EXPERIMENTAL RESULTS FOR CONCEPT DEMONSTRATION AND MODEL VALIDATION

This chapter presents the experimental results from the concept demonstrations and model validation efforts for the piezoelectric energy harvesting approaches explored. Two different types of lead zirconium titanate (PZT) harvesters were used in the experiments for this work – (a) T215-H4-503X PZT bimorphs (from Piezo Systems, Inc.) and (b) THUNDER® TH-6R transducer (originally developed by NASA Langley Research Center [42] and made commercially available by FACE International Corporation) which is a curved unimorph harvester. All experiments are performed over a range of 1-10 Hz to successfully capture the low frequencies inherent in human motion and ambient vibrations. A wide range of resistive loads are applied to the harvesters to capture the optimal loading scenario, but also successfully capture open circuit and short circuit conditions. First, frequency response functions were generated for both harvesters by exciting them over a range of frequencies and measuring the electromechanical response. Next, the bimorph is exposed to base excitations using a barrel shaker to validate the periodic base excitation model. Tuning of the resonant frequency of the bimorph using tip masses is simulated using a combination of measured data and the theoretical model. Using the linear bearings on a long stroke shaker, an experimental plucking set-up is created for the bimorph. Finally, a direct forcing set-up for the curved unimorph harvesters is created and used to validate the electromechanical model. The forcing levels are limited to 1-6 N due to the flattening of the curvature of the harvester.

4.1 Cantilevered Piezoelectric Bimorph under Periodic Base Excitation

The experimental set up along with a piezoelectric bimorph (Piezo Systems T215-H4-503X) can be seen in Figure 11. The bimorph harvester was clamped and fastened to a BK Type 4809 Vibration Exciter. A Laser Doppler Vibrometer was used to measure the tip velocity, while the acceleration at the base was measured using a Kistler 8636C50 accelerometer. A resistance box was used to apply a range of resistive loads across the output voltage from the harvester. The range of resistances was chosen to capture the optimal load resistance range. Finally, an NI-9223 data acquisition device was used to collect all the experimental measurements. The resulting fundamental short-circuit resonance frequency of the harvester was around 74.6 Hz, which becomes 78.8 Hz in open circuit as observed in Figure 12. The voltage and tip velocity were recorded for a range of load resistances and excitation frequencies and represented as FRFs shown in Figure 12. From these graphs it is clear there is very good agreement between the model and experimental data. Therefore, the bimorph piezoelectric energy harvesting model as reviewed in Section 3.1 can be confidently used for the specific excitation types (e.g. periodic excitation, plucking, etc.) in this work.

Table 2 – Relevant properties of Piezo Systems Bimorph (T215-H4-503X)

Piezoelectric Area [mm^2]	31.8×63.5	Weight [g]	8
Thickness [mm]	0.51	Piezoelectric Capacitance [nF]	92

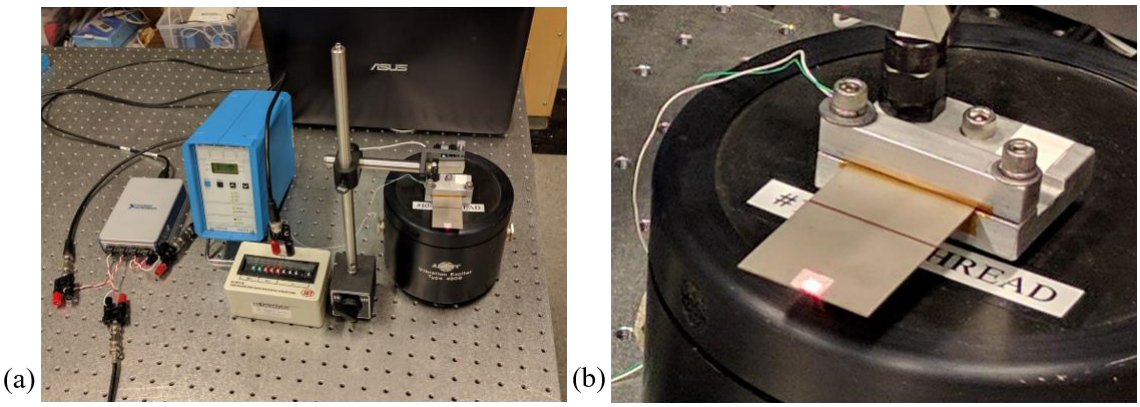

Figure 11 – (a) Base excitation experimental setup; (b) close-up of the bimorph harvester on vertical shaker

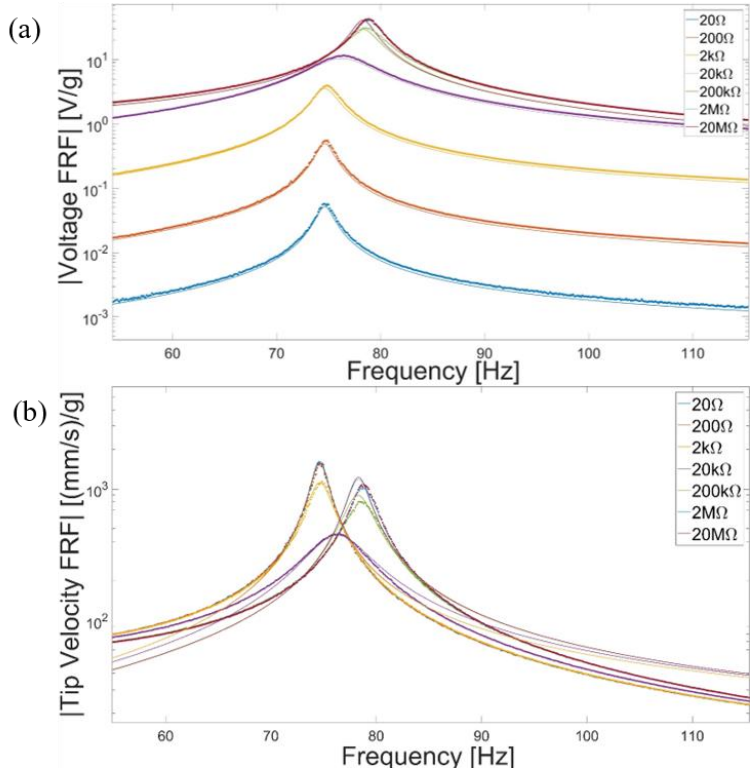

Figure 12 – Comparison of model and experimental (a) Voltage and (b) Tip Velocity FRFs for a range of load resistances (solid lines: model, dots: experiment)

To test the response of the model to low-frequency periodic excitations, the bimorph harvester is clamped to the armature of an APS-400 long stroke shaker. The shaker is provided with sinusoidal, saw tooth and square wave signals to represent irregular

periodic excitations. These excitations are applied over a range of 1-10 Hz to capture the low frequency range of human motion. The voltage output from the bimorph is measured across the same range of resistances used above. Base acceleration and tip velocity data are measured as before using an accelerometer and an LDV. Figure 13 shows the experimental setup for these tests.

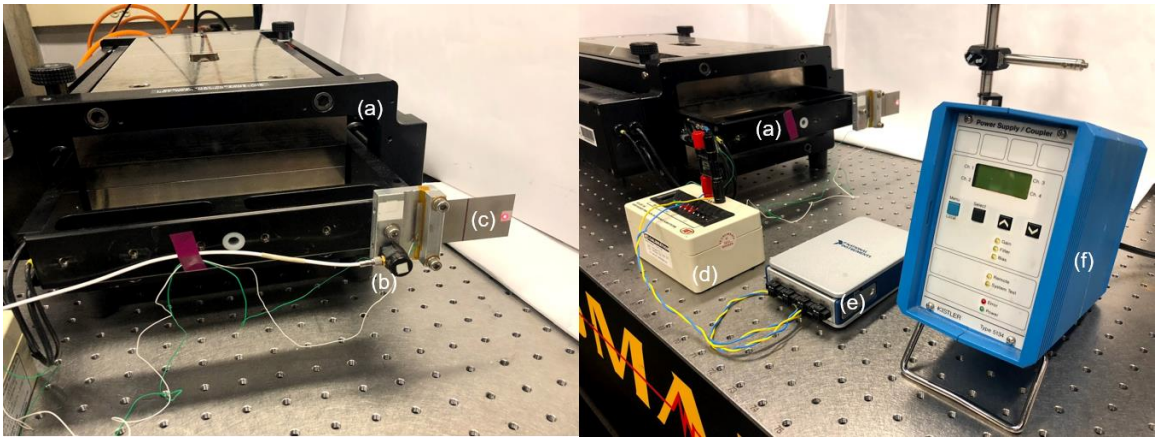

Figure 13 – Low-frequency periodic excitation experimental setup and close-up views: (a) Shaker; (b) accelerometer; (c) bimorph harvester; (d) resistance boxes; (e) NI-9223 data acquisition device; and (f) signal conditioner

A Fourier series expansion is performed on the measured base acceleration levels and used as the input to predict the electrical output from the harvester. The FRFs are used in Equations (14) – (16) to obtain the periodic electromechanical response of the harvester. Figure 14 shows the Fourier series representation of the base acceleration and the comparison of the experimental and theoretical voltage output for one excitation frequency (5 Hz) and one load scenario (200 kΩ).

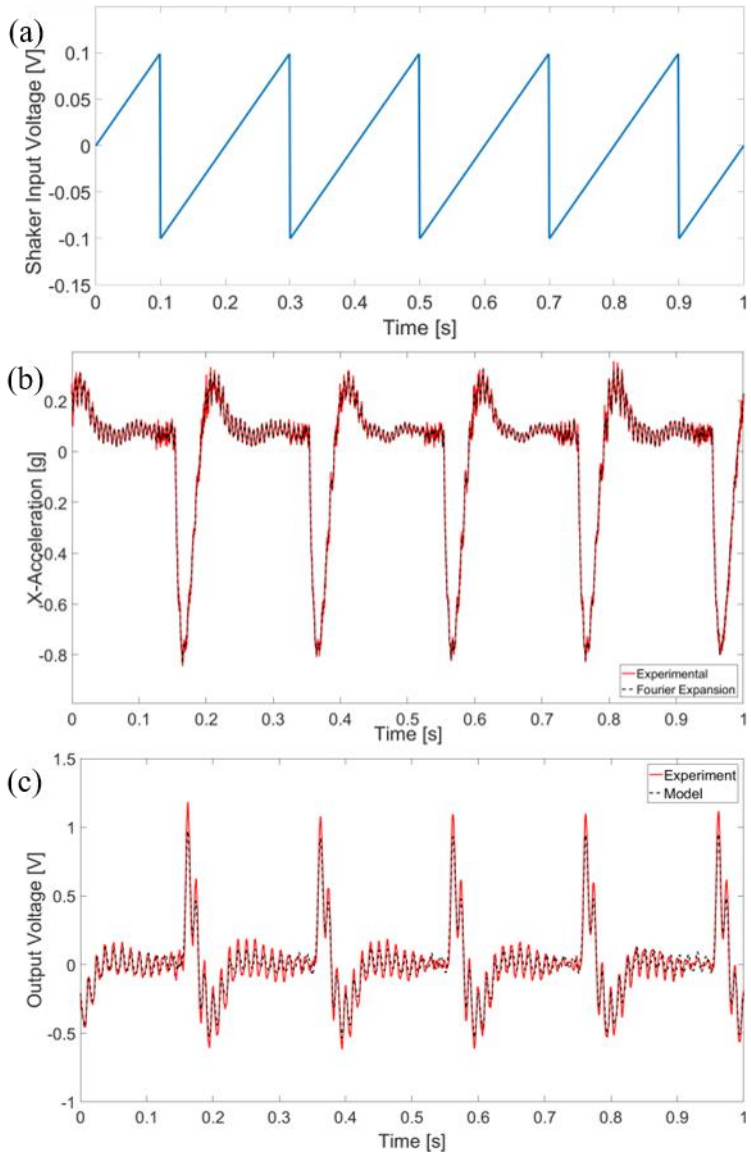

Figure 14 – (a) 5 Hz Saw tooth wave input to long stroke shaker (b) Comparison of measured base acceleration and Fourier series expansion for the input; (c) comparison of measured voltage and predicted voltage output versus time for the above signal over a 200 kΩ load resistance

The root-mean-square (RMS) value of the voltage time histories is used to estimate the average power output for the range of load resistances. Figure 15 compares analytically calculated values and the experimentally measured values for the RMS voltage and average power for the 5 Hz saw tooth excitation over the range of resistances used. There is very

good agreement between the model simulations and experimental measurements for electrical output from the harvester.

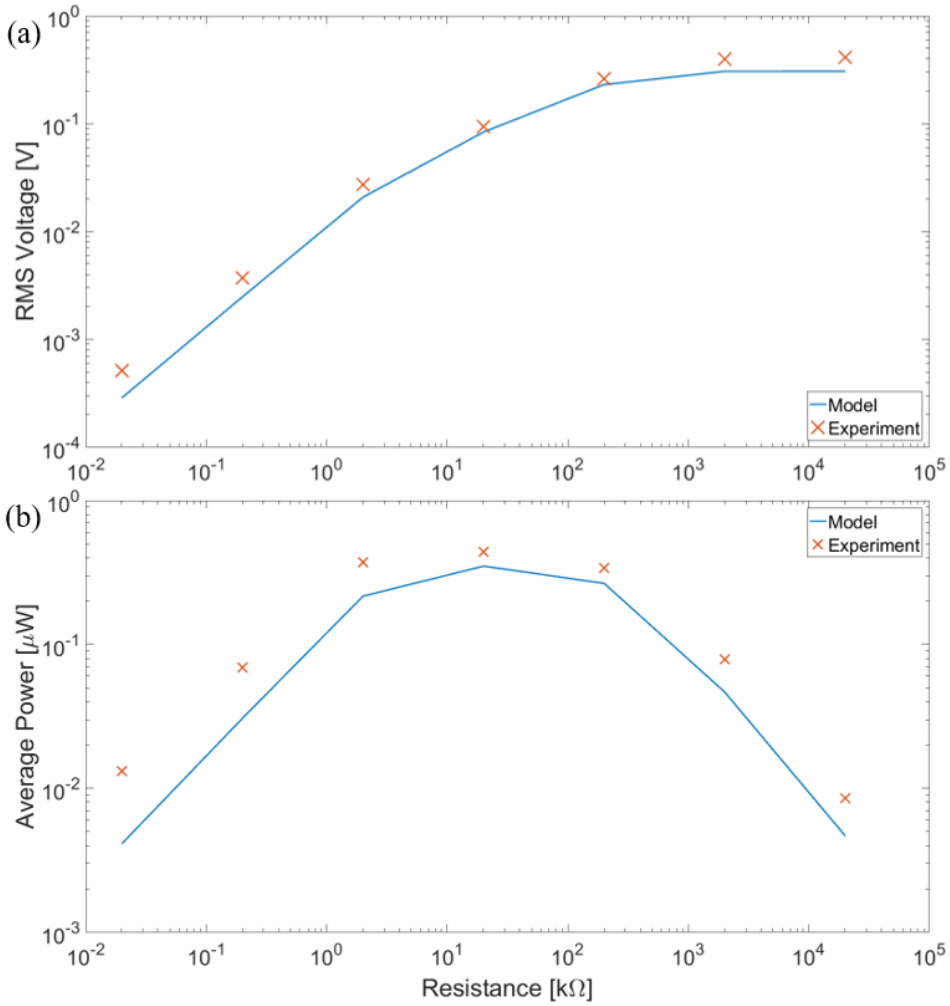

Figure 15 – Comparison of model predictions and experimental data for (a) RMS voltage and (b) Average power output

Using this validated electromechanical model and the period acceleration histories collected in Section 2.1, the electrical output is simulated for walking, jogging and sprinting. Figure 16, Figure 17 and Figure 18 show the output voltage time histories at the optimal load (20 kΩ) and average power output over a range of load resistances for the three excitation levels.

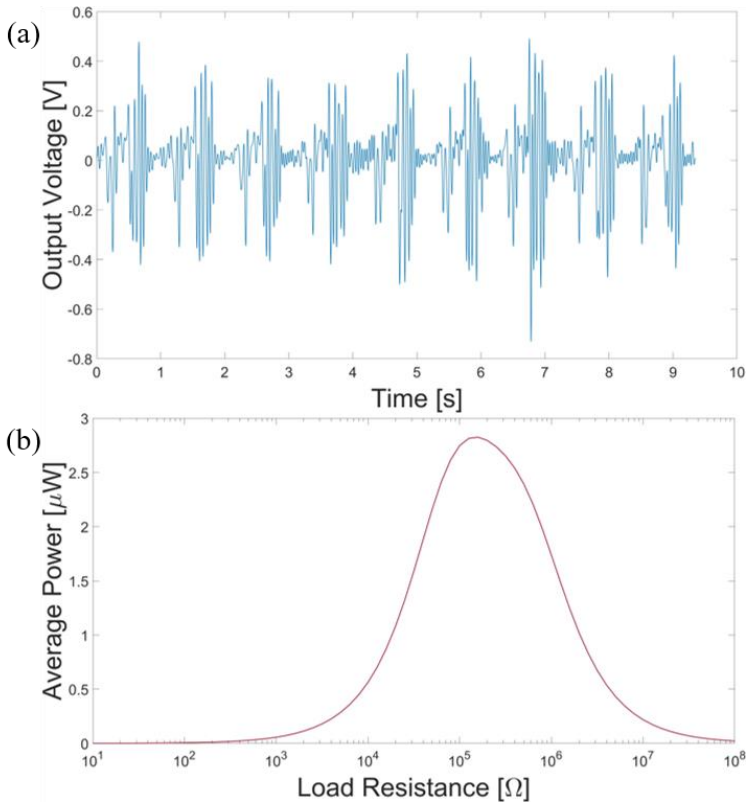

Figure 16 – (a) Output Voltage time history and (b) Average Power over a range of load resistances for walking excitation

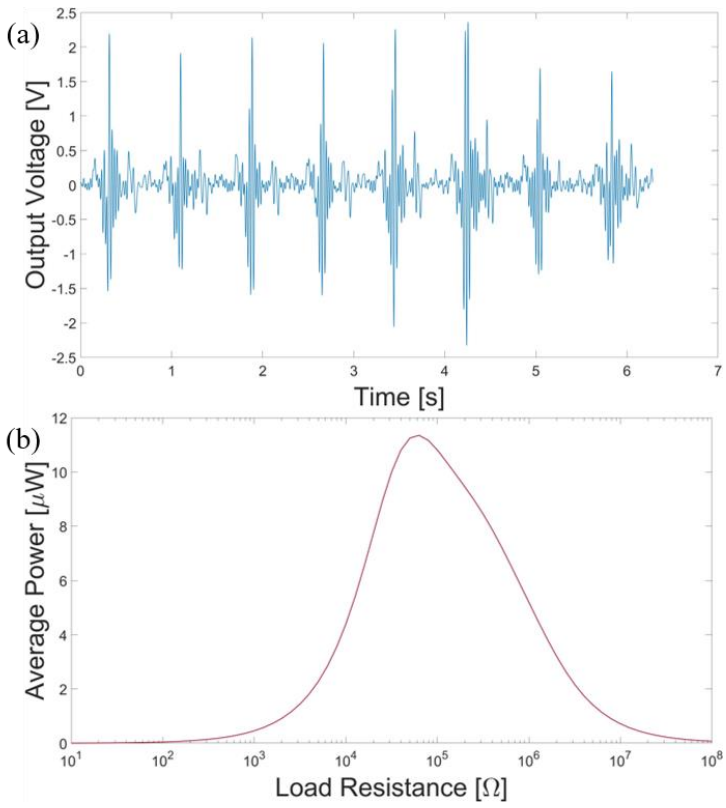

Figure 17 – (a) Output Voltage time history and (b) Average Power over a range of load resistances for jogging excitation

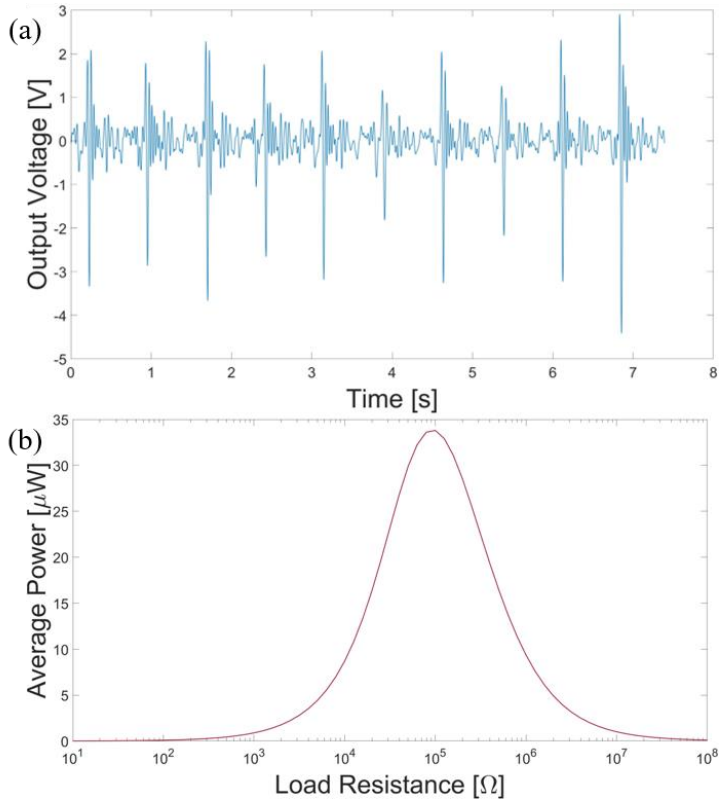

Figure 18 – (a) Output Voltage time history and (b) Average Power over a range of load resistances for sprinting excitation

It is observed that the optimal power output follows the expected trend of increasing with increased human motion pace. However, it is important to note that there is a significant mismatch between the excitation frequency content and the resonance frequency of the harvester used for these simulations (~ 75 Hz). This gap can be bridged by reducing the harvester's resonance frequency by adding tip mass. The resonance frequency of the cantilevered bimorph harvester is tuned to 25Hz, using a simulated 8.95 g mass, and 50 Hz, with a 1.42 g mass, in addition to the natural frequency of 75 Hz. Figure 19 compares the average power output possible with the tuned resonance frequencies of the harvester. As expected, the smaller the mismatch between the resonance frequency and the frequency content of the excitation, the higher the electrical output. It is important to

consider the deformation the designed harvesters experience under the human motion excitations. Figure 20 shows the maximum power and vibration levels of the three designs.

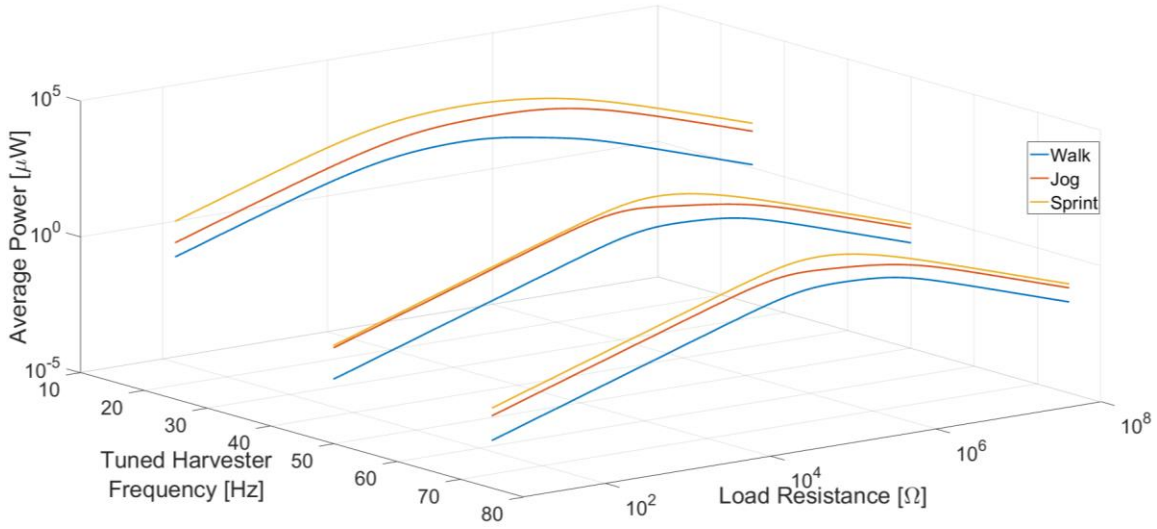

Figure 19 – Average Power output at the different tuned resonance frequencies (75Hz, 50Hz, 25Hz) of the harvester for the same excitation and load resistances

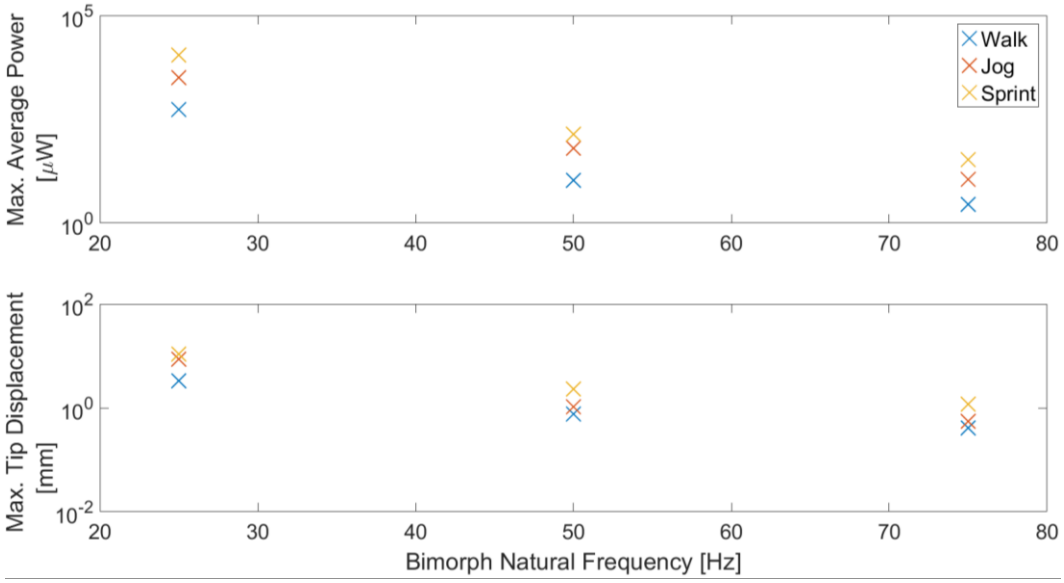

Figure 20 – Overall power and vibration levels of the three harvester designs for walking, jogging, and sprinting.

4.2 Plucked Piezoelectric Bimorph Harvester

The bimorph used in this set of experiments is the same as the one used in section 4.1, therefore the same electromechanical modeling parameters can be used in the analysis. Figure 21(a) shows the experimental setup for plucking-based energy harvesting, while Figure 21(b) depicts the deflection of the non-linear plectrum compared to the linear bimorph harvester during plucking excitations. A sheet of 0.05 mm (much thinner than the bimorph harvester) thick stainless steel is cut to the same width as the bimorph (31.8 mm) to be used as the nonlinear plectrum. The plectrum is clamped to the armature of a long stroke shaker, with the ability to slide the plectrum in the clamp to vary overlap length. The linear bearings in the long stroke shaker were used to ensure that the plucking motion is confined to the necessary direction. The plucking excitations are performed for a range of plectrum overlap lengths, 2 mm to 10 mm, and the electrical output is recorded over a range of load resistances, 20 Ω to 20 MΩ. The tip displacement of the harvester is measured using an LDV, while the output voltage from the harvester is recorded on an NI-4431 DAQ.

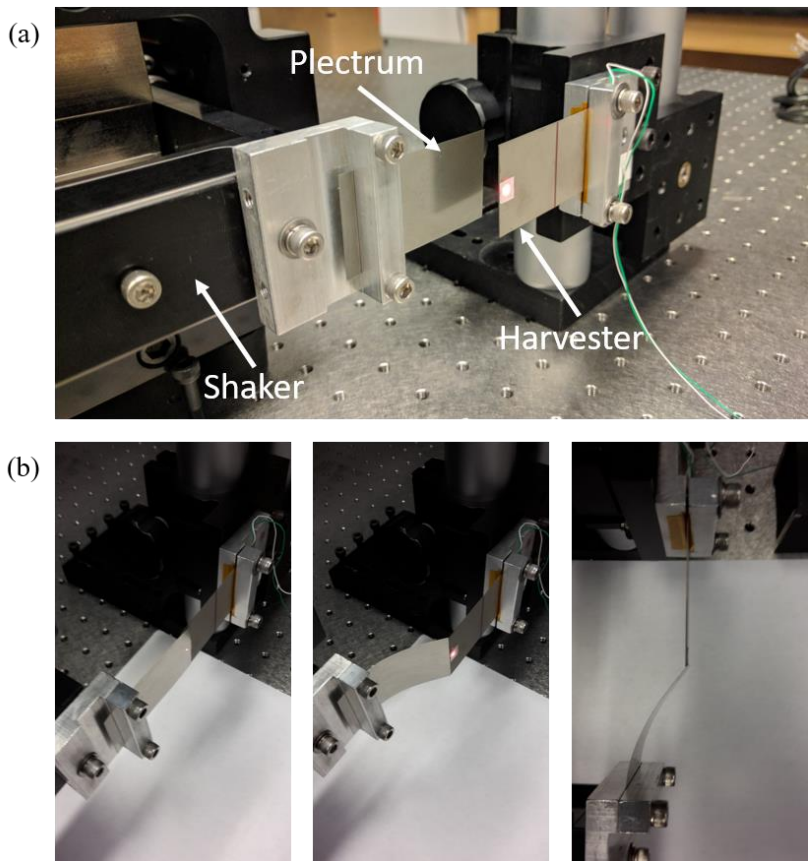

Figure 21 – (a) Experimental setup showing the bimorph harvester and the plectrum; (b) close up views of the plucking deformation of the geometrically nonlinear (flexible) plectrum compared to the geometrically linear (stiff) harvester

Combining the non-linear plectrum and the linear harvester model allowed for simulations of the voltage output and the tip velocity of the harvester. Figure 22 compares the voltage and tip velocity simulations to experimental data (at optimal electrical load, 20 kΩ) for the two extreme overlap lengths explored. There is very good agreement between the model simulations of voltage and tip velocity time series and the experimental measurements.

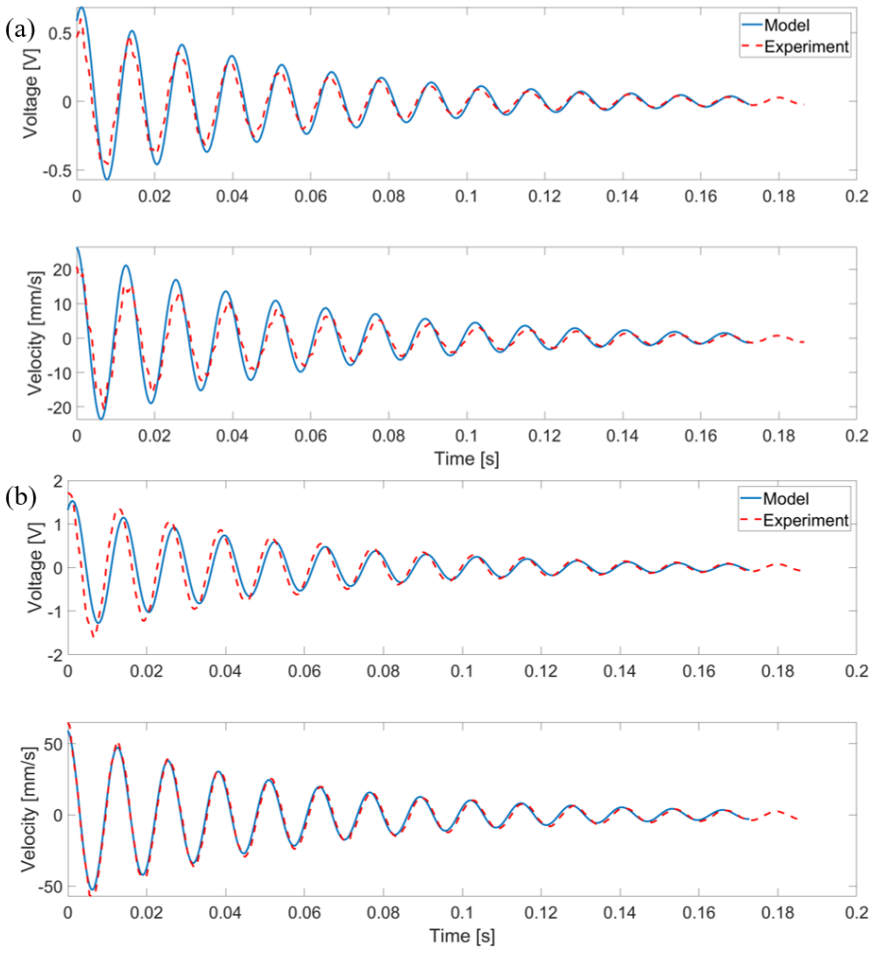

Figure 22 – Voltage and tip velocity time histories at the optimal load resistance of 20 kΩ for (a) 2 mm overlap and (b) 10 mm overlap

Once a plectrum and harvester are selected, the key input variable to the combined non-linear plectrum and linear harvester model is the overlap length *d*. Equation (38) describes the relationship between the overlap length *d* and the release height or initial tip deflection *h*. As expected, variation in the overlap length alters the initial tip deflection, and therefore also the initial tip force applied on the harvester. This relationship is described in Equation (45). Changing the applied initial tip force affects the harvested power output. This relationship between overlap length and harvested power is illustrated in Figure 23. Figure 24 highlights this relationship in the optimal resistive load scenario. It

is important to note the difficulty in successfully creating a zero-velocity initial condition in experiments, which is a major cause of the mismatch between model simulations and experimental data points. However, there is still a very good agreement between the two data sets.

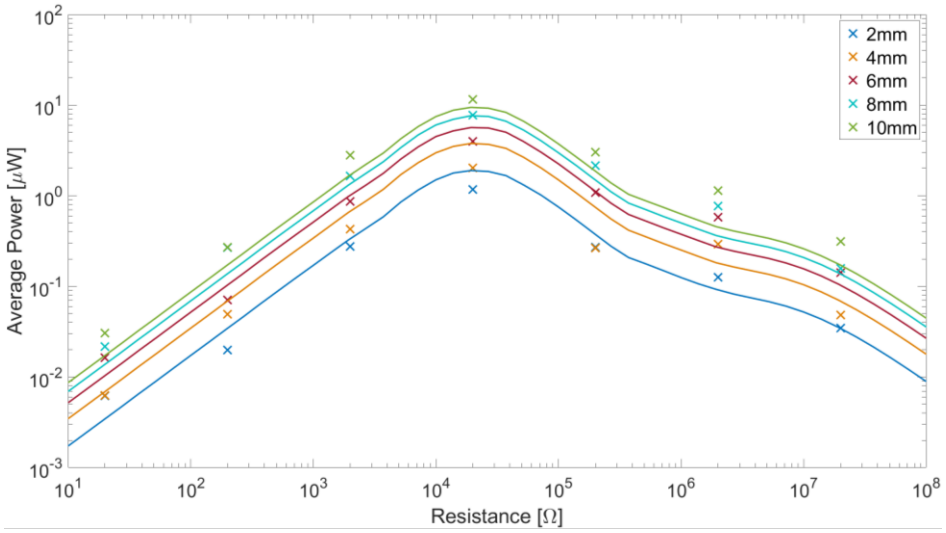

Figure 23 – Effect of overlap length on average power recorded over a range of load resistances (model simulations and experimental data)

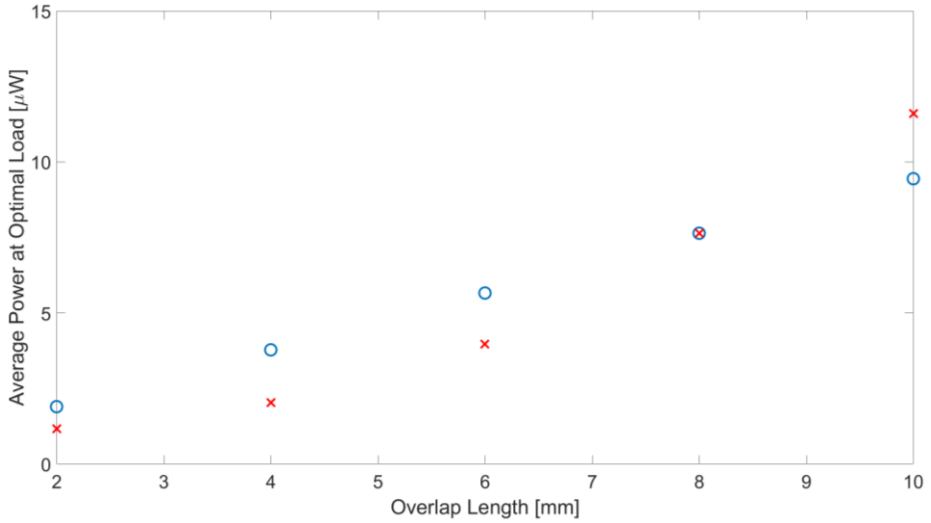

Figure 24 – Effect of overlap length on average power at optimal load resistance (20 kΩ)

With a validated electromechanical model, the effects on tip force and deflection as well as harvested power with variation of critical system parameters, such as the plectrum thickness and overlap length, are simulated for the same set up shown in Figure 21. The quasistatic transverse tip force transmitted to the harvester and corresponding harvester tip displacement are modeled as a function of plectrum thickness and overlap length. As expected, the harvester tip displacement follows a similar trend to the tip force. The maximum tip force of 0.21 N corresponding to a maximum tip deflection of 0.44 mm is seen when the plectrum thickness and overlap are at the maximum simulated values. The variation in tip force and tip deflection over the simulated parameter range can be seen in Figure 25. Increasing either the plectrum thickness or the overlap length would result in a higher force applied to the harvester. Note that the simulated tip displacement of the harvester is an order of magnitude lower than those seen in the bimorph under base excitation. The maximum tip displacement simulated does not exceed a value that would result in failure of the harvester.

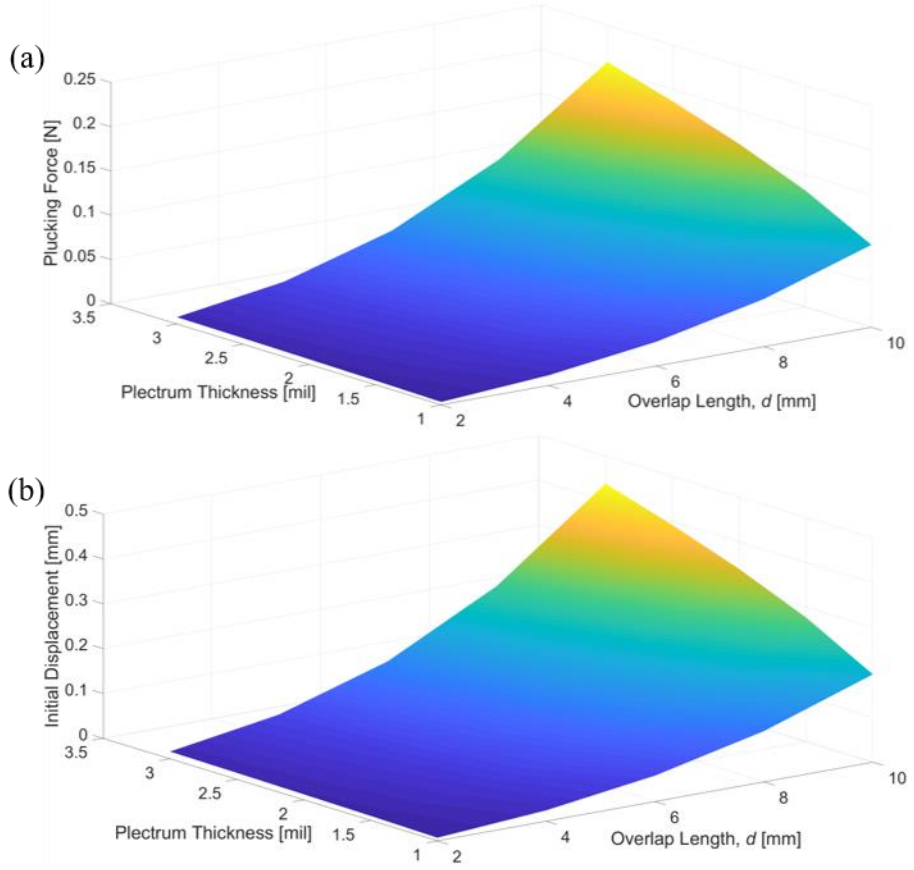

Figure 25 – Simulated (a) tip force and (b) initial tip displacement of the harvester with variation in plectrum thickness and overlap length

Next, the effect of varying system parameters on the electrical output is simulated. Increasing the overlap length and the plectrum thickness increases the average power output from the harvester. Figure 26 shows the variation in average power with plectrum thickness at the two extreme overlap length cases (2 mm and 10 mm). This trend is seen for all overlap lengths in Figure 27. Figure 28 shows the average power at optimal load increases by approximately 4 order of magnitude (0.15 µW to 108 µW) as the overlap increases from 2 mm to 10 mm.

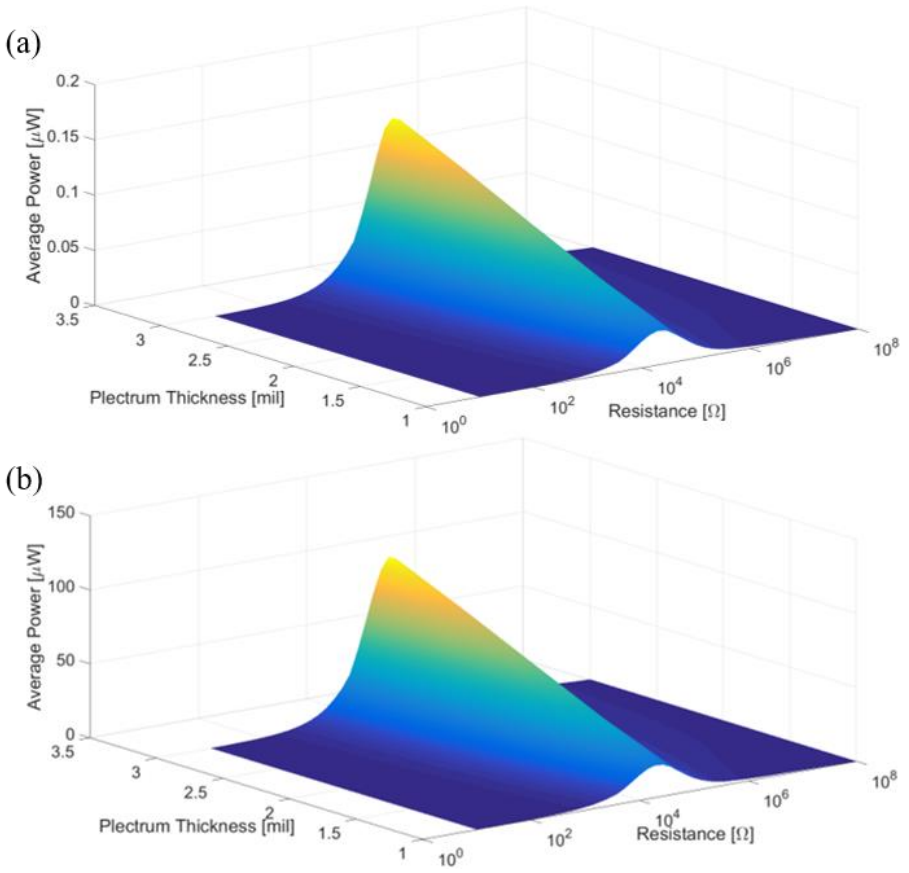

Figure 26 – Average power output versus plectrum thickness and load resistance for (a) 2 mm and (b) 10 mm overlap length

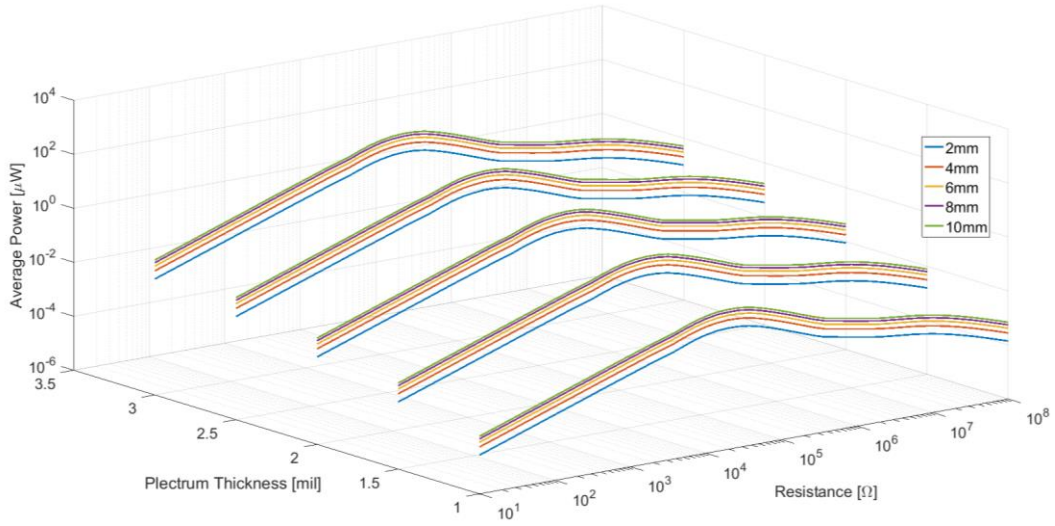

Figure 27 – Average power output for all simulated overlap lengths versus plectrum thickness and load resistance

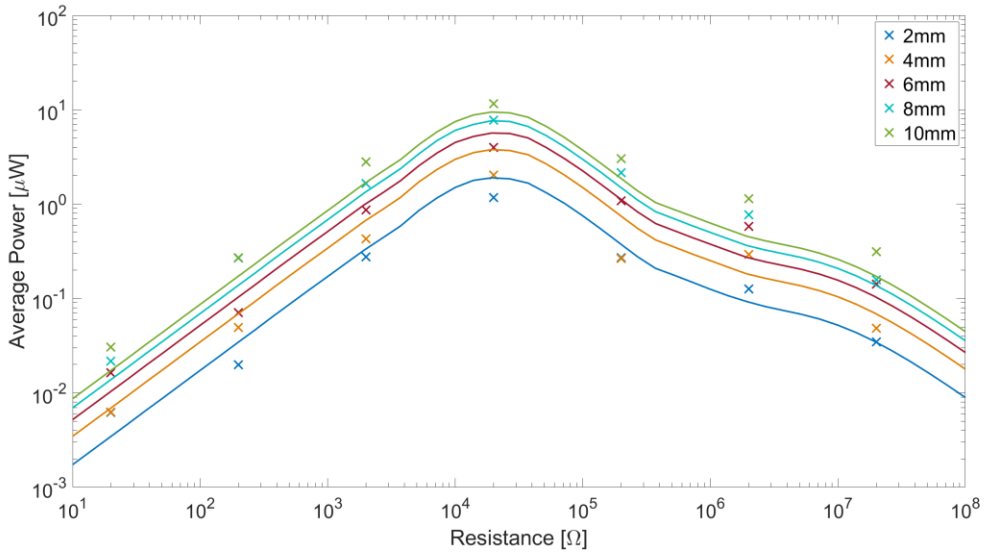

Figure 28 – Optimal power output (at 20kΩ) versus plectrum thickness for all overlap lengths

4.3 Curved Unimorph Harvester under Direct Force Excitation

The experimental setup used to characterize the THUNDER® TH-6R curved unimorph harvester is shown in Figure 29. The relevant properties of the sample used are listed in Table 3. To simulate simple boundary conditions (free to slide in 1-direction in Figure 10 to allow mechanical strain) the harvester is mounted to an acrylic base using four 4-40 screws. The base is attached to a Newport stand, and the harvester is horizontally compressed using an APS-400 long stroke shaker. A force transducer (PCB U0228D01), mounted to the top electrode of the harvester using magnets, is used to measure the force applied. A VCS201 controller is used to fix the applied force level over a range of frequencies. A resistive 1:10 voltage divider load across the sample is created using two resistance boxes. A range of load resistances were tested to capture the optimal load

resistance. An NI-9223 data acquisition device is used to record the force and voltage measurements.

Table 3 – Relevant properties of curved piezoelectric transducer (THUNDER® TH-6R)

Piezoelectric Area [mm^2]	50.8 × 50.8	Dome Height [mm]	4.24
Thickness [mm]	0.38	Piezoelectric Capacitance [nF]	68

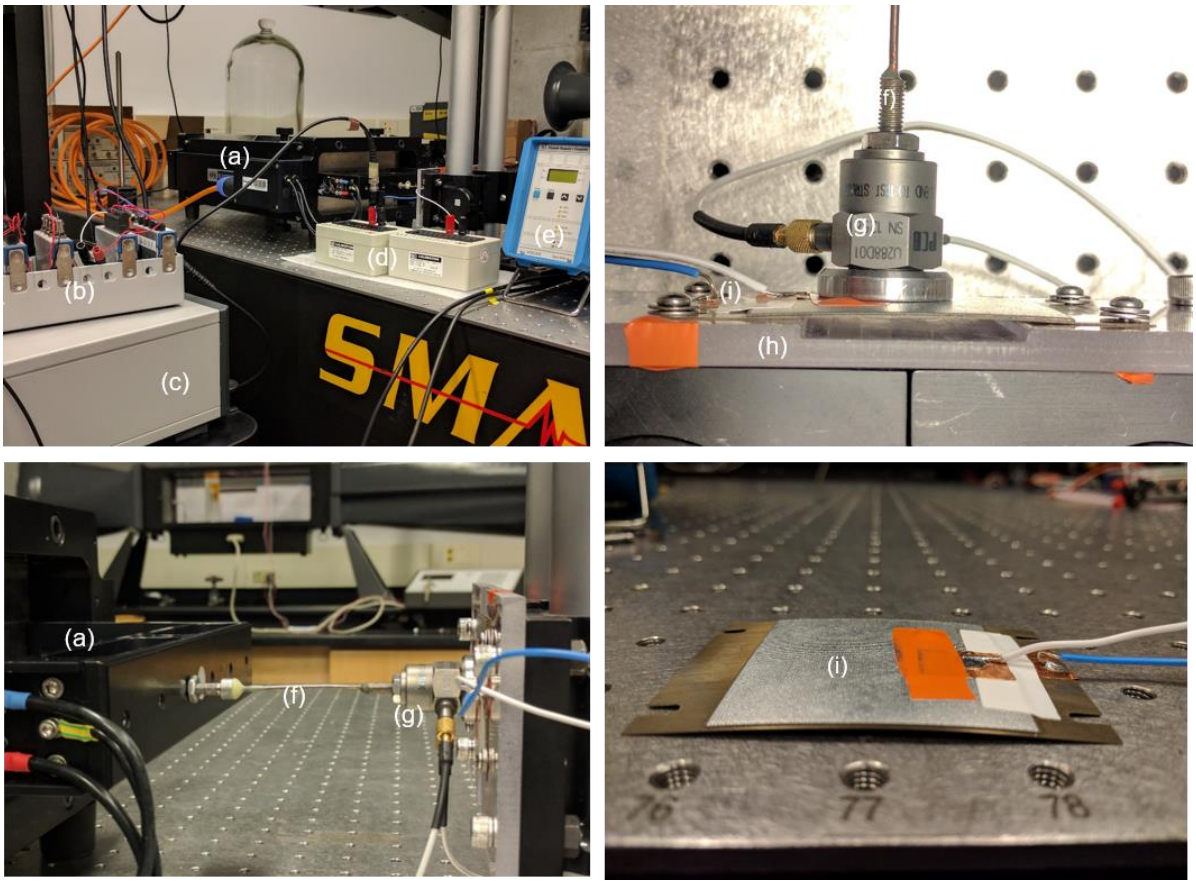

Figure 29 – Experimental setup and close-up views: (a) Shaker; (b) data acquisition hardware; (c) controller; (d) resistance boxes; (e) signal conditioner for the force transducer; (f) stinger; (g) force transducer; (h) acrylic mounting base; and (i) THUNDER® TH-6R harvester

The experiments attempt to represent the low frequencies inherent to human motion by focusing on a frequency range of 1-10 Hz. Using the controller to provide a specific

forcing amplitude, the harvester is subjected to harmonic excitations. It is noted that at RMS forcing levels of 8N caused the curved harvester to "bottom out" and become flat; limiting the experimental forcing levels from 1 to 7 N. The voltage output is measured across a range of load resistances (100 kΩ, 250 kΩ, 300 kΩ, 500 kΩ and 750 kΩ). The RMS voltage output is calculated across these load resistances for each forcing level. The experimental measurements are compared to theoretical solutions simulated using the frequency response functions represented by Equations (53) and (54) from the model developed in Section 3.4. The value for the electromechanical coupling term (θ) is computed for a specific case as 2.929×10^{-7} C/N. The equivalent capacitance of the THUNDER® element is measured experimentally to be 68 nF. For a given excitation frequency (in rad/s), the optimal load resistance is $1/\omega C_p$.

Figure 30 shows the voltage and power frequency response curves in 3D and 2D. In these figures, the experimental output to input ratio is extracted at all force levels to confirm repeatability. A close agreement is seen between the trends predicted by the analytical model and the experimental results, and the fixed set of system parameters (θ, C_p) successfully represented the governing dynamics of the curved piezoelectric energy harvester. Any error seen is likely due to the change in the nominal static equilibrium position as the excitation force level or frequency changed.

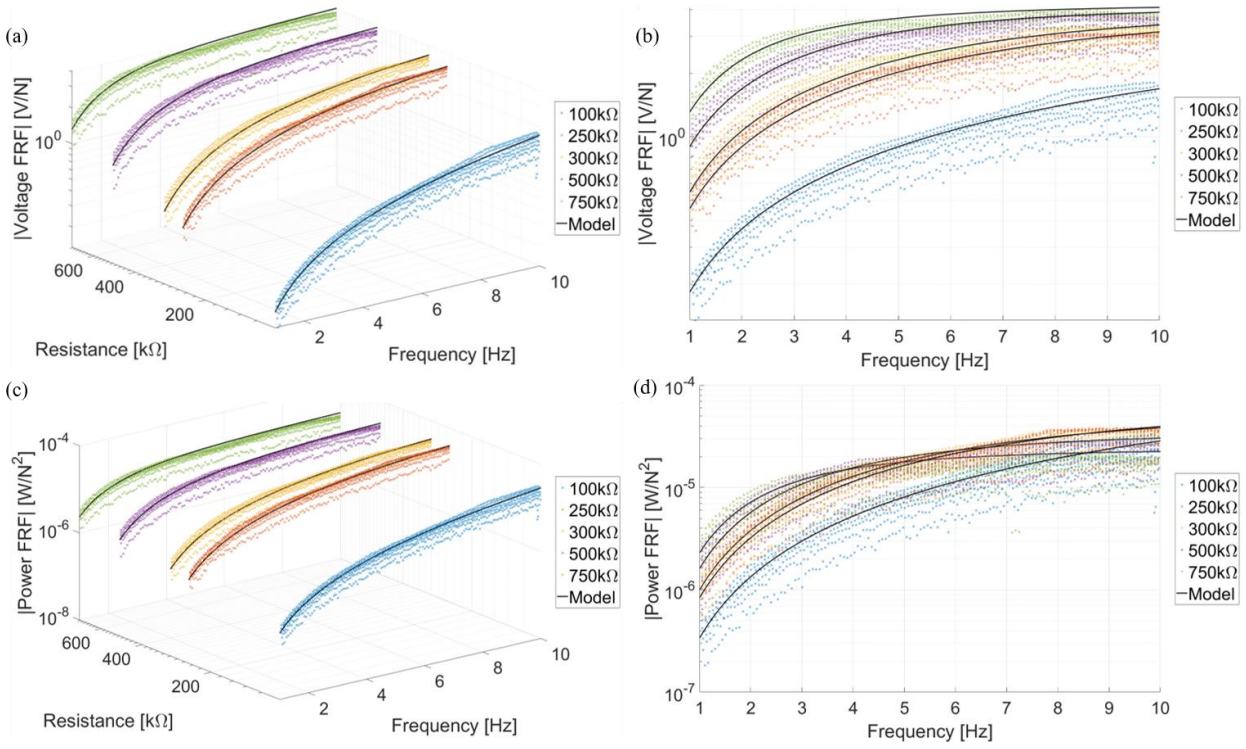

Figure 30 – (a) Voltage output-to-force input FRFs and (b) Power output-to-force input FRFs of the THUNDER® TH-6R energy harvester for the tested range of load resistances

The average power is calculated using the RMS voltage. Both these values are then plotted versus the different RMS force levels applied to the harvester. In the model developed for a curved unimorph harvester, Equations (53) and (54) describe a linear relationship between voltage and force, whereas the power is proportional to the square of the force. Figure 31 and Figure 32 compare the experimentally measured values of RMS voltage and average power to the RMS forcing levels applied to the harvester. A clear linear dependence between voltage and force is observed in Figure 31 and the quadratic relationship between power and force can be seen in Figure 32. The large deviations between the model and experiment at higher frequencies can be attributed to potential nonlinearities that are beyond the scope of this work.

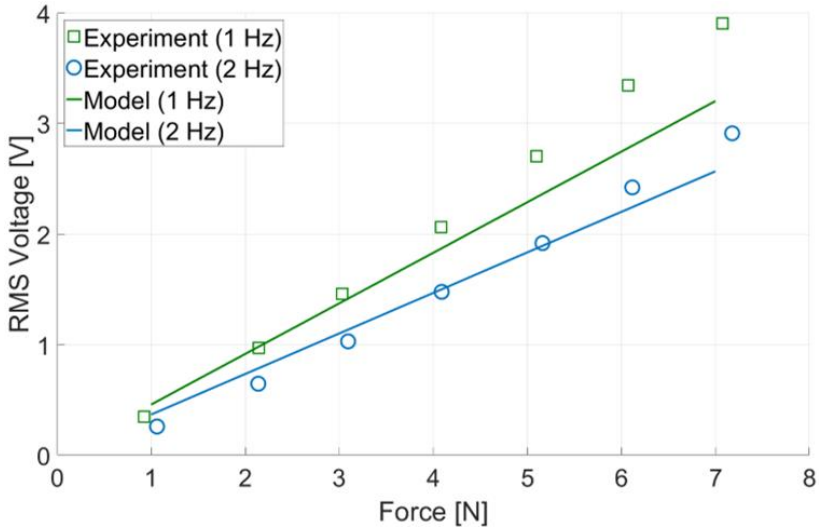

Figure 31 – RMS Voltage output levels for various RMS force levels at 1 Hz (250 kΩ) and 2 Hz (for 100 kΩ)

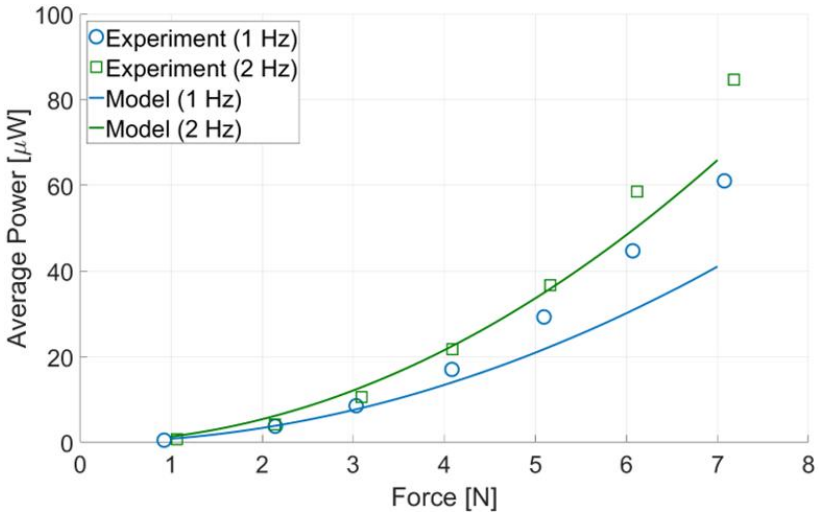

Figure 32 – Average power output levels for various RMS force levels at 1 Hz (250 kΩ) and 2 Hz (for 100 kΩ)

Next, similar to the bimorph case, the model for the curved unimorph harvester is experimentally validated for periodic excitations. Using the same experimental setup as before, a saw tooth direct forcing excitation is applied to the THUNDER® TH-6R harvester. The experimental forcing levels (RMS) used for this set of experiments is 1-6 N with a frequency of 1-10 Hz. The electrical output is recorded over 20 different resistance

values from 1 kΩ to 2 MΩ. Figure 33 highlights the time history of the electric response for the 1N loading scenario at two different excitation frequencies (1 and 2 Hz). A very good agreement is observed between the experimentally voltage time histories and the voltage output predicted by the model. Figure 34 and Figure 35 show the relationship between the RMS amplitude of the saw tooth direct force excitation and the electrical output.

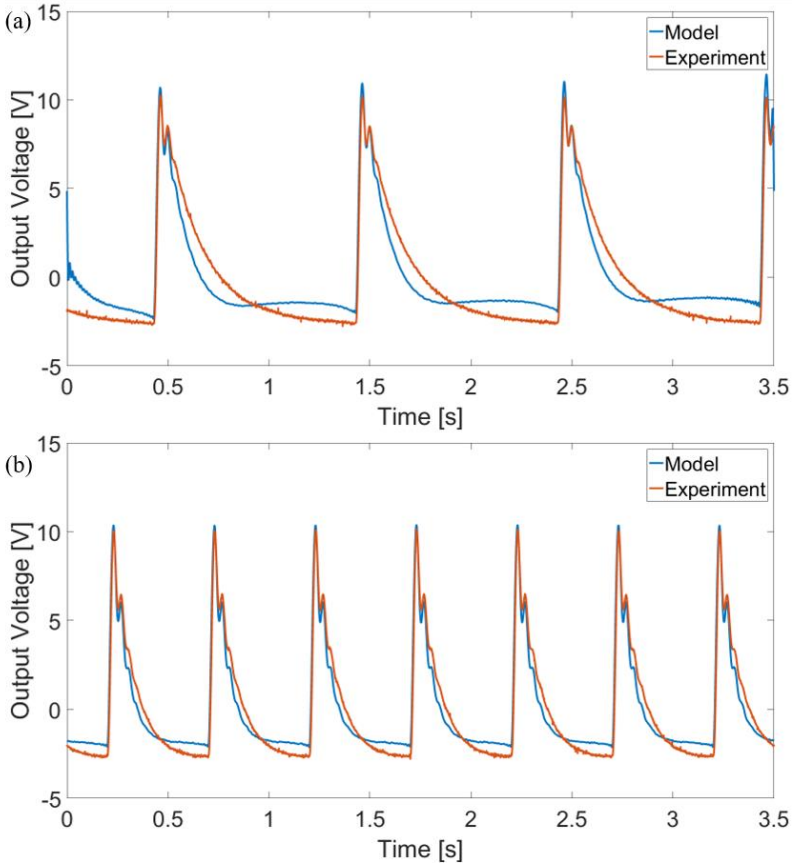

Figure 33 – Comparison of (a) experimentally measured voltage time histories and the model for 1 N forcing at (a) 1 Hz (Load resistance 2 MΩ and (b) 2 Hz (Load resistance 1 MΩ)

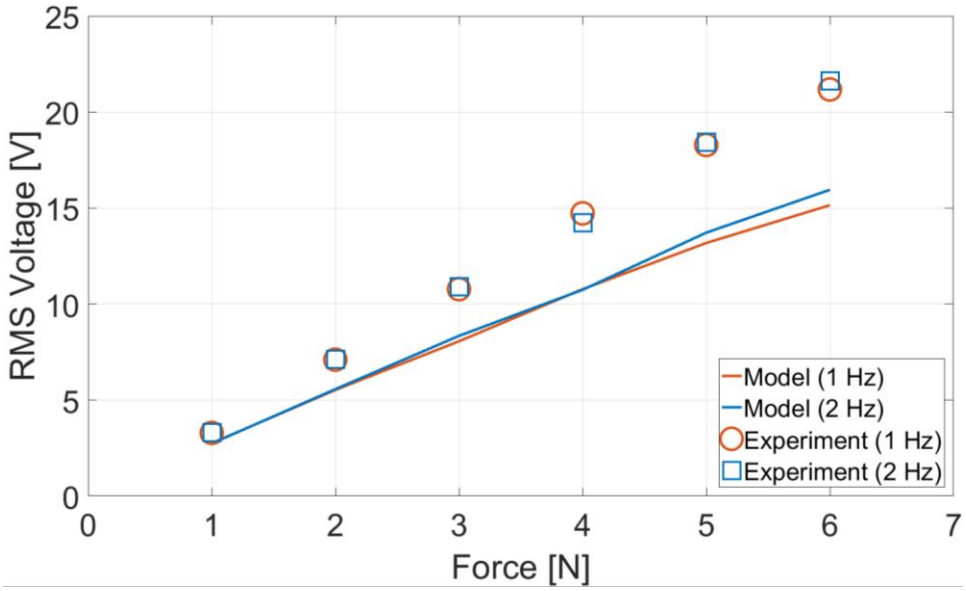

Figure 34 – RMS Voltage output levels for various RMS force levels at 1 Hz (2 MΩ) and 2 Hz (for 1 MΩ)

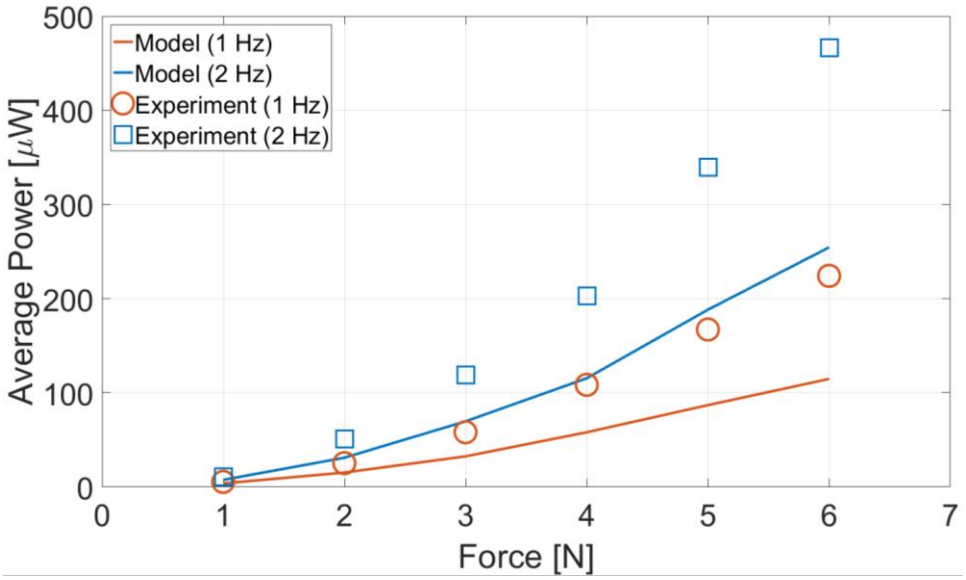

Figure 35 – Average power output levels for various RMS force levels at 1 Hz (2 MΩ) and 2 Hz (for 1 MΩ)

This fully validated electromechanical for curved unimorph harvesters can now be used to be predict the theoretical maximum power generation capability of human motion. The periodic force histories recorded in Section 2.2 are used as the input to the direct

forcing model and the electrical output is simulated for walking, jogging and sprinting. Figure 36, Figure 37, and Figure 38 show the output voltage time histories at 1000 kΩ and the average power output over a range of load resistances for the three excitation histories.

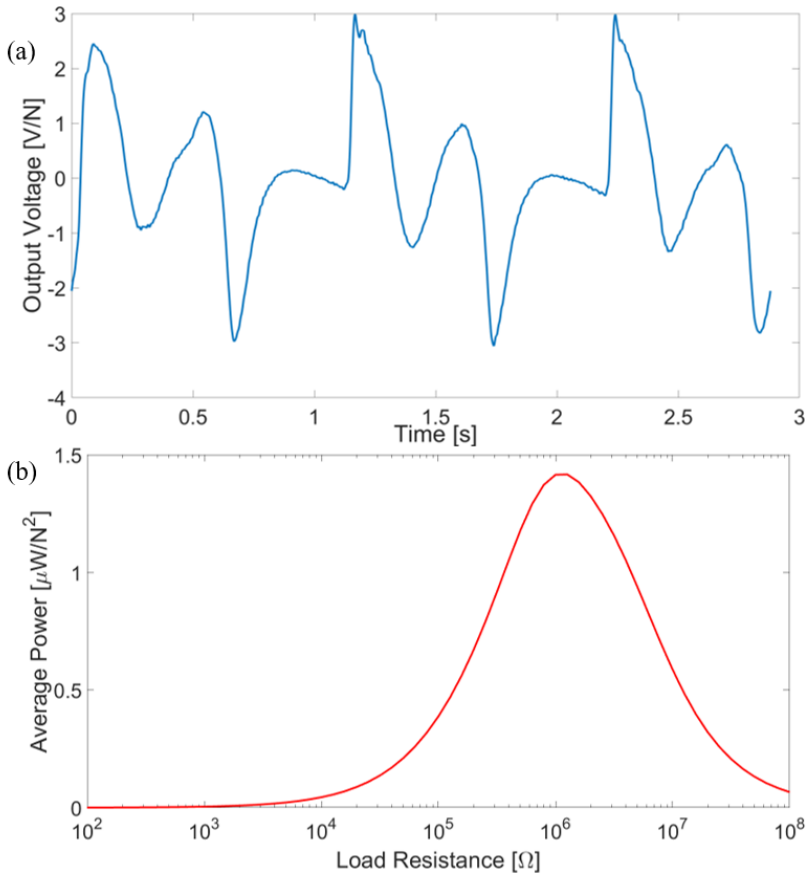

Figure 36 – (a) Output Voltage time history and (b) Average Power over a range of load resistances for walking excitation

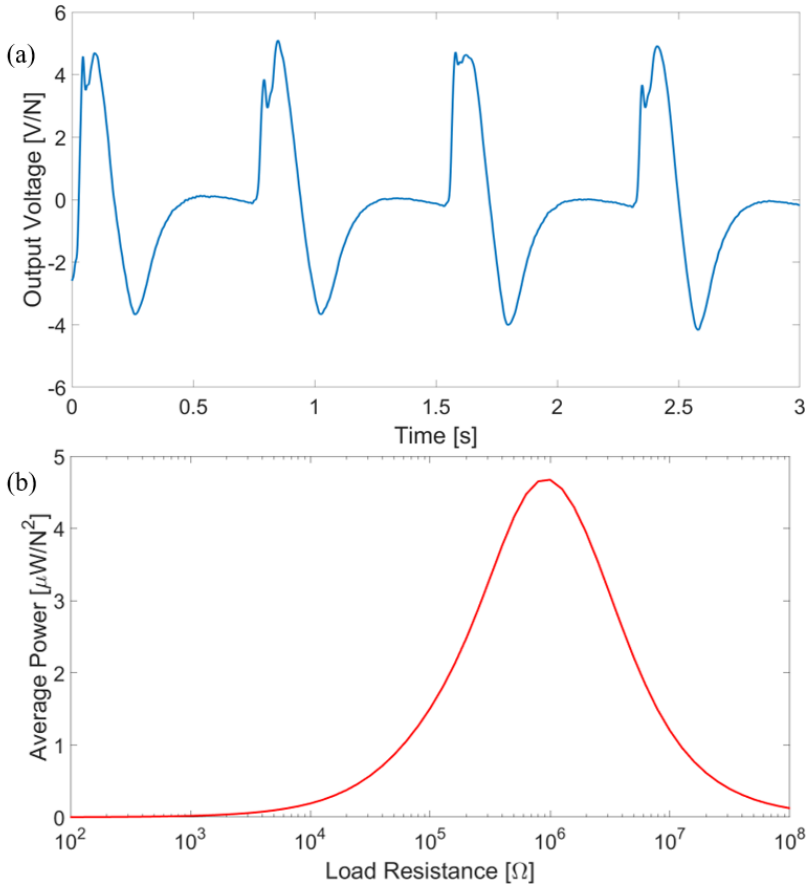

Figure 37 – (a) Output Voltage time history and (b) Average Power over a range of load resistances for jogging excitation

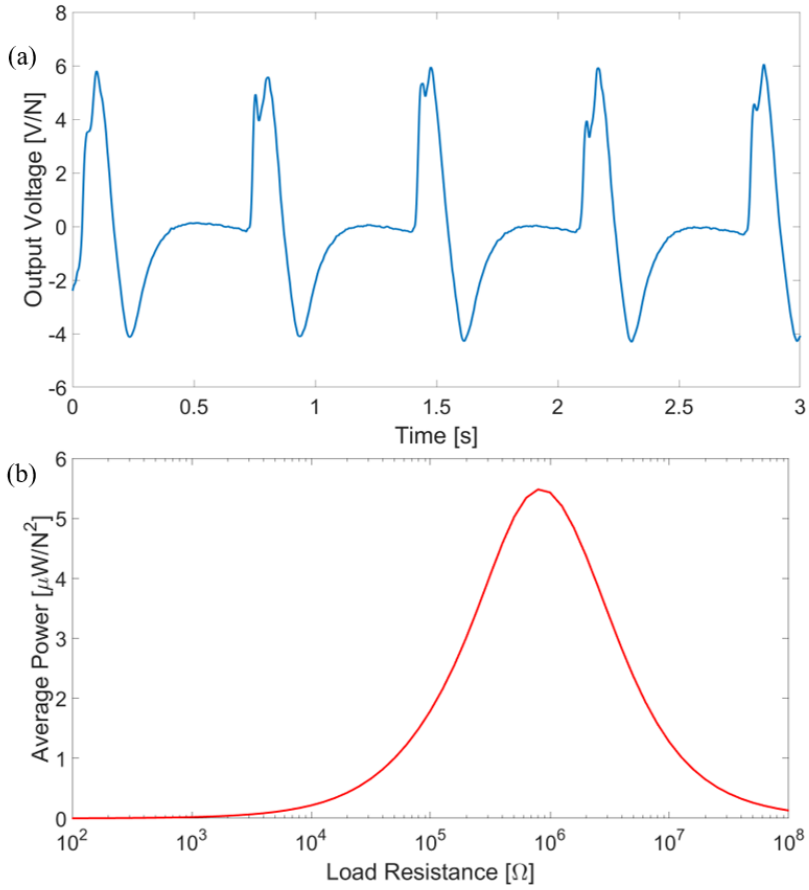

Figure 38 – (a) Output Voltage time history and (b) Average Power over a range of load resistances for sprinting excitation

Again, it is observed that the optimal power output follows the trend of increasing with increased human motion pace – like in the case of the bimorph under base excitation. However, it is important to consider that the forcing amplitudes recorded during human motion are much higher than what is required to collapse (bottom-out) or even shatter the piezoelectric layer on the curved unimorph. Therefore, while the model predicts that power on the order of Watts can be harvested using this configuration, it ignores the deformation of the harvester. This issue can be mitigated by stacking multiple elements, thereby increasing the maximum load the stack can withstand or with novel load transfer mechanisms that protect the energy harvesters.

CHAPTER 5. CONCLUSIONS

This thesis explored various architectures for piezoelectric energy harvesting from human body motions. Analytical models for voltage and power output from three different harvester configurations were developed and experimentally validated. Specifically, piezoelectric transduction for the scenarios of (1) direct base excitation of cantilevered bimorph configuration without/with a tip mass; (2) plucking of a bimorph cantilever using a flexible/nonlinear plectrum; and (3) direct force excitation of a curved unimorph (THUNDER® configuration) were explored. Table 4 shows the maximum power outputs of various excitation mechanisms and piezoelectric energy harvesting methods, including periodic excitation of bimorphs, plucking case, curved unimorph under direct forcing. Overall, it has been shown in this work that the experimental results closely follow the trends seen in the analytical models. The higher error seen for the curved unimorph configuration are attributed to potential nonlinearities that are beyond the scope of this work. Typical average power output levels are on the order 10-100 μW and can easily exceed milli-Watts in certain cases.

Table 4 – Experimental data vs. model predictions of the maximum power output for the optimal electrical load for different excitation methods

	Excitation Type	Experiment	Model
Piezo Systems Bimorph (T215-H4-503X)	**Saw Tooth Base Excitation**	3.95 $\mu W/g^2$	3.14 $\mu W/g^2$
	Plucking	2657.29 $\mu W/N^2$	2629.76 $\mu W/N^2$
FACE Corporation THUNDER® TH-6R	**Harmonic Direct Forcing (1 Hz)**	0.95 $\mu W/N^2$	0.84 $\mu W/N^2$
	Harmonic Direct Forcing (2 Hz)	1.17 $\mu W/N^2$	1.34 $\mu W/N^2$
	Saw Tooth Direct Forcing (1 Hz)	13.23 $\mu W/N^2$	6.10 $\mu W/N^2$
	Saw Tooth Direct Forcing (2 Hz)	6.46 $\mu W/N^2$	7.13 $\mu W/N^2$

Using the validated electromechanical models and measured human body acceleration and force levels, predictions are made for the maximum power harvesting capabilities of these harvesters. Table 5 compiles the predictions made for energy harvesting from a cantilevered bimorph under base excitation and the direct forcing of a curved unimorph. The models predict usable power on the scale of micro-watts for the bimorph, and watts for the curved unimorph harvester. However, the curved unimorph model does not consider the deformation of the harvester, and therefore the actual power harvested will likely be much lower. It is seen that both configurations result in micro-watt level power generation per unit acceleration or force. Improvements in the efficiency of piezoelectric energy harvesting along with development of associated architectures could result in an increase to milli-watt level power generation.

Table 5 – Modeled theoretical maximum power output from human loads applied to (a) base excited bimorph and (b) curved unimorph under direct forcing

	(a) Base Excitation of Bimorph		(b) Direct Forcing of Curved Unimorph	
	Average Power at Optimal Load (μW)	**Power FRF ($\mu W/g^2$)**	**Average Power at Optimal Load (W)**	**Power FRF ($\mu W/N^2$)**
Walk (3 mph)	0.52	0.34	0.34	0.53
Jog (5 mph)	11.63	0.69	2.13	0.85
Sprint (7 mph)	21.78	0.45	2.67	0.86

REFERENCES

[1] S. P. Beeby, M. J. Tudor, and N. White, "Energy harvesting vibration sources for microsystems applications," *Measurement science and technology,* vol. 17, no. 12, p. R175, 2006.

[2] S. Anton, K. Farinholt, and A. Erturk, "Piezoelectret foam–based vibration energy harvesting," *Journal of Intelligent Material Systems and Structures,* vol. 25, no. 14, pp. 1681-1692, 2014.

[3] K. Cook-Chennault, N. Thambi, and A. Sastry, "Powering MEMS portable devices—a review of non-regenerative and regenerative power supply systems with special emphasis on piezoelectric energy harvesting systems," *Smart Materials and Structures,* vol. 17, no. 4, p. 043001, 2008.

[4] K. A. Cunefare, E. Skow, A. Erturk, J. Savor, N. Verma, and M. Cacan, "Energy harvesting from hydraulic pressure fluctuations," *Smart Materials and Structures,* vol. 22, no. 2, p. 025036, 2013.

[5] A. Erturk and D. J. Inman, *Piezoelectric Energy Harvesting*. Chichester, UK: John Wiley & Sons, 2011.

[6] S. Leadenham and A. Erturk, "M-shaped asymmetric nonlinear oscillator for broadband vibration energy harvesting: Harmonic balance analysis and experimental validation," *Journal of Sound and Vibration,* vol. 333, no. 23, pp. 6209-6223, 2014.

[7] J. L. González, A. Rubio, and F. Moll, "Human powered piezoelectric batteries to supply power to wearable electronic devices," *International journal of the Society of Materials Engineering for Resources,* vol. 10, no. 1, pp. 34-40, 2002.

[8] C. Corporation, "Advanced Power Solutions for Wearable Technology and Internet of Everything Sensors," ed, 2014.

[9] C. B. Williams, C. Shearwood, M. A. Harradine, P. H. Mellor, T. S. Birch, and R. B. Yates, "Development of an electromagnetic micro-generator," (in English), *Iee Proceedings-Circuits Devices and Systems,* vol. 148, no. 6, pp. 337-342, Dec 2001.

[10] P. Glynne-Jones, M. J. Tudor, S. P. Beeby, and N. M. White, "An electromagnetic, vibration-powered generator for intelligent sensor systems," (in English), *Sensors and Actuators a-Physical,* vol. 110, no. 1-3, pp. 344-349, Feb 1 2004.

[11] P. D. Mitcheson, P. Miao, B. H. Stark, E. M. Yeatman, A. S. Holmes, and T. C. Green, "MEMS electrostatic micropower generator for low frequency operation," (in English), *Sensors and Actuators a-Physical,* vol. 115, no. 2-3, pp. 523-529, Sep 21 2004.

[12] L. G. W. Tvedt, D. S. Nguyen, and E. Halvorsen, "Nonlinear Behavior of an Electrostatic Energy Harvester Under Wide- and Narrowband Excitation," (in English), *Journal of Microelectromechanical Systems,* vol. 19, no. 2, pp. 305-316, Apr 2010.

[13] S. Roundy and P. K. Wright, "A piezoelectric vibration based generator for wireless electronics," (in English), *Smart Materials & Structures,* vol. 13, no. 5, pp. 1131-1142, Oct 2004.

[14] N. E. duToit and B. L. Wardle, "Performance of microfabricated piezoelectric vibration energy harvesters," (in English), *Integrated Ferroelectrics,* vol. 83, pp. 13-32, 2006.

[15] N. S. Shenck and J. A. Paradiso, "Energy scavenging with shoe-mounted piezoelectrics," *IEEE micro,* vol. 21, no. 3, pp. 30-42, 2001.

[16] A. Erturk and D. J. Inman, "An experimentally validated bimorph cantilever model for piezoelectric energy harvesting from base excitations," *Smart materials and structures,* vol. 18, no. 2, p. 025009, 2009.

[17] D. Benasciutti, L. Moro, S. Zelenika, and E. Brusa, "Vibration energy scavenging via piezoelectric bimorphs of optimized shapes," *Microsystem technologies,* vol. 16, no. 5, pp. 657-668, 2010.

[18] X. Z. Dai, Y. M. Wen, P. Li, J. Yang, and X. F. Jiang, "A Vibration Energy Harvester Using Magnetostrictive/Piezoelectric Composite Transducer," (in English), *2009 Ieee Sensors, Vols 1-3*, pp. 1374-1377, 2009.

[19] J. Hu, F. Xu, A. Q. Huang, and F. G. Yuan, "Optimal design of a vibration-based energy harvester using magnetostrictive material (MsM)," (in English), *Smart Materials & Structures,* vol. 20, no. 1, Jan 2011.

[20] M. Aureli, C. Prince, M. Porfiri, and S. D. Peterson, "Energy harvesting from base excitation of ionic polymer metal composites in fluid environments," (in English), *Smart Materials & Structures,* vol. 19, no. 1, Jan 2010.

[21] R. D. Kornbluh *et al.*, "From boots to buoys: Promises and challenges of dielectric elastomer energy harvesting," (in English), *Electroactive Polymer Actuators and Devices (Eapad) 2011*, vol. 7976, 2011.

[22] S. Boisseau, G. Despesse, T. Ricart, E. Defay, and A. Sylvestre, "Cantilever-based electret energy harvesters," *Smart Materials and Structures,* vol. 20, no. 10, p. 105013, 2011.

[23] Q. Deng, M. Kammoun, A. Erturk, and P. Sharma, "Nanoscale flexoelectric energy harvesting," *International Journal of Solids and Structures,* vol. 51, no. 18, pp. 3218-3225, 2014.

[24] A. G. Moura and A. Erturk, "Electroelastodynamics of flexoelectric energy conversion and harvesting in elastic dielectrics," *Journal of Applied Physics,* vol. 121, no. 6, p. 064110, 2017.

[25] L. Moro and D. Benasciutti, "Harvested power and sensitivity analysis of vibrating shoe-mounted piezoelectric cantilevers," *Smart Materials and Structures,* vol. 19, no. 11, p. 115011, 2010.

[26] M. Pozzi and M. Zhu, "Plucked piezoelectric bimorphs for knee-joint energy harvesting: modelling and experimental validation," *Smart Materials and Structures,* vol. 20, no. 5, p. 055007, 2011.

[27] M. Pozzi and M. Zhu, "Characterization of a rotary piezoelectric energy harvester based on plucking excitation for knee-joint wearable applications," *Smart Materials and Structures,* vol. 21, no. 5, p. 055004, 2012.

[28] P. Pillatsch, E. Yeatman, and A. Holmes, "Magnetic plucking of piezoelectric beams for frequency up-converting energy harvesters," *Smart Materials and Structures,* vol. 23, no. 2, p. 025009, 2013.

[29] P. Pillatsch, E. M. Yeatman, and A. S. Holmes, "A piezoelectric frequency up-converting energy harvester with rotating proof mass for human body applications," *Sensors and Actuators A: Physical,* vol. 206, pp. 178-185, 2014.

[30] S. Wei, H. Hu, and S. He, "Modeling and experimental investigation of an impact-driven piezoelectric energy harvester from human motion," *Smart Materials and Structures,* vol. 22, no. 10, p. 105020, 2013.

[31] D. A. Barton, S. G. Burrow, and L. R. Clare, "Energy harvesting from vibrations with a nonlinear oscillator," *Journal of Vibration and Acoustics,* vol. 132, no. 2, p. 021009, 2010.

[32] S. Leadenham and A. Erturk, "Nonlinear M-shaped broadband piezoelectric energy harvester for very low base accelerations: primary and secondary resonances," *Smart Materials and Structures,* vol. 24, no. 5, p. 055021, 2015.

[33] A. Toprak and O. Tigli, "Piezoelectric energy harvesting: State-of-the-art and challenges," *Applied Physics Reviews,* vol. 1, no. 3, p. 031104, 2014.

[34] F. Duarte and A. Ferreira, "Energy Harvesting on Road Pavements," presented at the Advances in Civil, Structural and Environmental Engineering, 2015.

[35] M. Alwan *et al.*, "A smart and passive floor-vibration based fall detector for elderly," in *Information and Communication Technologies*, 2006, vol. 1, pp. 1003-1007.

[36] A. Morales, "Paris marathon to harvest runners' energy with PaveGen tiles," *Bloomberg Business,* 2013.

[37] B. Kathpalia, D. Tan, I. Stern, F. Valdes, S. Kim, and A. Erturk, "Modeling and Characterization of a Curved Piezoelectric Energy Harvester for Smart Paver Tiles," *Procedia Computer Science,* vol. 109, pp. 1060-1066, 2017.

[38] B. Kathpalia, D. Tan, I. Stern, and A. Erturk, "An experimentally validated model for geometrically nonlinear plucking-based frequency up-conversion in energy harvesting," *Smart Mater. Struct,* vol. 27, no. 015024, p. 015024, 2018.

[39] C. L. Dym and I. H. Shames, *Solid mechanics*. Springer, 1973.

[40] "Standards Committee of the IEEE Ultrasonics, Ferroelectrics, and Frequency Control Society, IEEE Standard on Piezoelectricity," (in English), *ANSI/IEEE Standard on Piezoelectricity 176-1987,* pp. 1-66, 1984.

[41] S. Zhao and A. Erturk, "Deterministic and band-limited stochastic energy harvesting from uniaxial excitation of a multilayer piezoelectric stack," *Sensors and Actuators A: Physical,* vol. 214, pp. 58-65, 2014.

[42] R. G. Bryant, "Overview of NASA Langley's piezoelectric ceramic packaging technology and applications," *NASA Report 20080000875* 2007.